

Atomistic Simulations of Atomic Force Microscopy

Inauguraldissertation

zur

Erlangung der Würde eines Doktors der Philosophie

vorgelegt der

Philosophisch–Naturwissenschaftlichen Fakultät

der Universität Basel

von

Seyed Alireza Ghasemi

aus Karaj, Iran

Basel, 2010

Genehmigt von der Philosophisch-Naturwissenschaftlichen Fakultät
auf Antrag von:

Prof. Dr. Stefan Goedecker

Prof. Dr. Ernst Meyer

Basel, 24 June 2008

Prof. Dr. Hans-Peter Hauri

To my parents and my wife

Contents

1	Introduction	1
2	Novel Computational Methods for Calculating the Coulomb Interaction	5
2.1	Particle-Particle, Particle-Scaling Method	7
2.2	The Results of the P^3S Method	9
2.3	Particle-Particle, Particle-Density Method	12
2.3.1	Coulomb interaction for systems with periodic boundary conditions in two dimensions and free in the other one	13
2.3.2	Calculating the long range part	15
2.3.3	Solving the ordinary differential equation using the finite element method	18
2.4	Numerical Results	19
2.4.1	Numerical results for the Poisson solver	20
2.4.2	Numerical results for point particles	21
2.4.3	Energy conservation	22
2.4.4	The optimal method parameters	22
2.5	Conclusion	24
3	Candidates for Silicon Tip Structures	25
3.1	Si-H Tight-Binding Scheme	27
3.2	Search Algorithms for Low-Energy Structures	29

3.2.1	Overview on global optimization methods	30
3.2.2	Minima hopping method	31
3.2.3	Why minima hopping method?	32
3.3	Silicon Tip Structures	33
3.3.1	Small silicon model tips	34
3.3.2	Medium-size partially H-passivated Si cluster $Si_{70}H_{50}$	37
3.3.3	Medium-size partially H-passivated Si clusters $Si_{71}H_{50}$	40
3.3.4	Medium-size partially H-passivated Si clusters $Si_{72}H_{50}$	43
3.3.5	Large partially H-passivated Si clusters ($Si_{238}H_{118}$)	45
3.3.6	A Si cluster on a reconstructed Si(001) 2×1 surface	49
3.3.7	The stiffness of the investigated model tips	53
3.3.8	Discussion	56
3.3.9	Conclusion	57
4	Ubiquitous Mechanisms of Energy Dissipation in Noncontact Atomic Force Microscopy	59
4.1	Introduction	59
4.2	Investigating Energy Dissipation in NCAFM Using More Realistic Model Tips	61
4.3	Conclusion	67
5	Conclusions and Outlook	69
A	The Details of the System of Linear Equations for the P^3D Method.	73

Chapter 1

Introduction

An important milestone in exploration of physical phenomena on the nanometer scale was the invention of scanning tunneling microscopy (STM) in 1982 by G. Binig and H. Rohrer [1]. Later the field of scanning probe microscopy (SPM) opened up a new horizon in this exploration. Using atomic force microscopy (AFM), invented in 1986, [2], atomic resolution has been achieved so far on a variety of surfaces [132, 101, 102, 103]. Non-contact atomic force microscopy (NCAFM) [132] has become an established technique in nanoscience which, unlike scanning tunneling microscopy, can resolve atomic-scale features even on insulating samples. Typical atomic force microscopes are capable of measuring interaction forces down to the piconewton range. A microfabricated cantilever with a sharp tip at its end serves as a force sensor. Normal and lateral forces on the tip are measured as bending and twisting of the cantilever.

In dynamic non-contact measurements, the cantilever is excited at its resonance frequency. During the oscillations, the tip approaches the surface so that attractive forces dominate the tip-sample interactions. The free oscillation frequency of the cantilever is influenced by the tip-surface interaction resulting in a frequency shift. There are two ways to measure this frequency shift. One is based on amplitude detection where the cantilever is excited at a frequency close to the resonance frequency (AM-mode or tapping mode) [3]. If the eigenfrequency is shifted due to the tip-sample interaction force gradient, the amplitude is changing and can be used as a feedback parameter to scan over the surface. In the frequency modulation mode (FM-mode) [4], the cantilever is excited at its eigenfrequency and a feedback loop keeps the amplitude constant. The frequency shift, which arises due to the tip-sample interaction, is typically used as a feedback parameter to control the tip-sample distance while scanning.

The interaction forces between the tip and the surface can be separated into chemical short-range forces with an interaction length of a fraction of nm and long range forces, which extend up to 100 nm. The long range capillary forces can be neglected in the UHV. The long range Van der Waals forces act between the mesoscopic tip end and the surface,

while the long range electrostatic forces interact with the whole cantilever. Therefore, the long range forces can be described as an interaction between macroscopic bodies. In contrast, the short-range forces take place between very few atoms of the tip-apex and the surface atoms. These forces provide information on the sample down to the atomic scale. The fact that in AFM different parts of the tip and cantilever contribute differently to the total force and thus feedback signal, respectively is in strong contrast to the STM, where only the foremost atoms contribute to the tunneling current. The contribution of the outermost tip atoms dominates the tunneling current due to the strong exponential decay with the distance. On the other hand, the interplay of the different forces in AFM complicates the interpretation of the topographic measurements. Due to this complicated nature of the tip-sample interaction forces, it took a decade for atomic force microscopy to mature into a true atomic scale tool.

Using atomic force microscopy, high-resolution images of DNA, proteins and polymers have been obtained in air and liquids [5, 6, 7, 8, 9]. True atomic resolution images of several semiconductor and insulator surfaces [103, 10, 11] have also been reported. AFM applications are not limited to the scanning of surface topography. The applicability of AFM ranges from high-resolution imaging of biomolecules and polymers, large-scale patterning of silicon surfaces to the study of friction in the nanometer scale and the manipulation of single nanoparticles. Recent studies have proven that controlled manipulation of individual atoms is also possible using NCAFM [69]. These capabilities will, e.g. enable quantitative studies of externally triggered conformational changes of individual molecules assembled on various substrates.

Although both the long-range and the short-range forces act between the tip and the sample surface, eventually only the short-range forces are of interest due to their contribution of high-resolution in NCAFM and atom manipulation and so on. For this reason, a good understanding of the tip-apex structures is indispensable to the scientists in the field of scanning probe microscopy. Nowadays, this information is hardly obtained by the experiments, only atomistic simulations are able to provide detailed insight into the tip-apex structures and also the atomic relaxations processes induced by the tip-sample interaction. However the problem is very complex indeed, the lack of experimental information leaves many variables unknown in a system presenting a very intricate energy landscape. To tackle this problem we need efficient, fast but still accurate tools.

One theoretical approach to study the AFM experiments is to model it for a specific purpose, e.g. one can describe qualitatively the frictional stick-slip tip lateral motion by the Tomlinson model. Unfortunately modeling is feasible provided the model parameters are known from the experiments or the atomistic simulations. On the other hand, many pieces of information can hardly be obtained by experiments, only atomistic simulations provide detailed insights. For example, atomistic simulations are currently the only approach to investigate the nanometer scale tip-apex structures. However, the use of atomistic simulation is also problematic since an accurate treatment of the particles is computationally very expensive. Only the latest generation of computers have made

realistic atomistic simulations possible.

There are several different approaches, from classical approaches to quantum ones, which can be used for the interaction between the particles, however, only some of them are both efficient and accurate enough for a specific system to be used in an AFM simulation. For example, force field methods are accurate enough for ionic systems in order to calculate many quantities in an AFM simulation while they are not accurate enough for silicon systems. In this dissertation, recently developed methods such as P^3S , P^3D , and a new Si-H tight-binding scheme are presented. These methods will be of great help for the atomistic simulations of the atomic force microscopy. The Coulomb interaction is dominant in ionic systems so that the accurate and efficient evaluation of Coulomb interactions is crucial for the atomistic simulations of the ionic systems such as alkali halides, etc. The previously used methods for calculating the Coulomb interaction are not suitable for the simulation of isolated surfaces or surface interacting with AFM tips. These systems can properly be investigated by having periodic boundary conditions in the two directions and free boundary condition in the third one abbreviated to 2DP1DF. The P^3D method does a remarkable job, very efficiently and accurately and without restrictions, in the calculation of the Coulomb interaction with 2DP1DF boundary conditions which is fully compatible with the surface problems. This method is currently being used for potassium bromide and sodium chloride systems, however, the results are not presented in this dissertation.

The Si-H tight-binding scheme used in this thesis is a generalization of the previously introduced Si tight-binding scheme of T. Lenosky which is one of the most successful tight-binding models for the treatment of Si atoms. The Si-H tight-binding scheme has been used in several global optimization calculations for searching the low energy structures of constrained H-terminated Si clusters as model tips. The global optimization technique used in our calculations is the minima hopping method. Several different constrained clusters with different sizes have been studied as well as a silicon cluster on the reconstructed Si(001) 2×1 surface. These results are presented in the chapter three.

Atomic scale dissipation is of great interest in nanomechanics and atomic manipulation. To investigate energy dissipation in the AFM experiments, we used some of the model tips, presented in chapter three, in a number of atomic force microscopy simulations. The novel energy dissipation mechanisms arising from an AFM tip are described in chapter four. The use of more realistic model tips, such as those found in the global optimization calculations, in atomic force microscopy simulations, is vital to reveal unknown processes in an atomic force microscopy experiment.

Finally in the chapter five, we summarize the results of our investigations presented in the chapters two, three and four.

In summary, the objective of the present work is to study atomic force microscopy by means of atomistic simulations. To this aim, we developed efficient techniques which enable us to perform a systematic search of Si possible tip-apex structures. This sheds

some light on the atomic structure of the apexes of the Si tips used by the dynamic force microscopy.

Chapter 2

Novel Computational Methods for Calculating the Coulomb Interaction

Force field methods (also known as molecular mechanics) ignore the electronic degrees of freedom and calculate the energy of a system as a function of the nuclear positions only. Molecular mechanics is used to perform calculations on systems containing a significant number of atoms. In some cases force fields can provide answers that are sufficiently accurate or even comparable with the high-level quantum mechanical calculation, in a fraction of the computer time. However, molecular mechanics cannot of course provide properties that depend upon the electronic distribution in a molecule.

The fast and accurate calculation of Coulomb interaction is one of the most challenging tasks in the simulations of charged particles in force field methods. This challenge arises from the periodicity in one, two or three dimensions, usually required in simulations, as well as the long range nature of Coulomb interaction. So far an enormous number of methods has been developed for the four possible types of boundary conditions(BC). A desired method should have properties such as (i) $\mathcal{O}(N)$ complexity, (ii) the approximate forces to be exact derivatives of the approximate energy, (iii) a large increase in accuracy at the cost of a small increase in calculation time, (iv) easy to implement, (v) high capability of parallelizability.

Two types of geometries are of interest in simulations of scanning probe microscopy (SPM). One is the isolated system to simulate SPM tips as cluster models in stand-alone mode. The other is the slablike geometry to simulate the sample alone or together with the tip. Slablike geometry also appears in problems involving electrolyte solutions between charged surfaces, proteins near charged membranes, thin films of ferrofluids, interfaces, surfaces, tip-surface interaction in scanning probe microscopy simulations, Wigner crystals, charged films, membranes, etc. These systems can be well simulated by periodic BC in two dimensions and finite(free) in the third, abbreviated as 2DP1DF. On the other

hand the appropriate BC to simulate isolated molecules and clusters is the free BC in all the three dimensions, abbreviated by 3DF.

In the following an overview of the different general approaches for calculating Coulomb interaction is given briefly with their advantages and limitations.

Ewald-type Methods The famous Ewald sum does a remarkable job in splitting the very slowly converging sum over the Coulomb potential into two sums, one in the real space and the other in Fourier space, which both converge rapidly. Ewald method can be optimized, for a given accuracy, from scaling $\mathcal{O}(N^2)$ to $\mathcal{O}(N^{\frac{3}{2}})$ [12, 13] but only for the three dimensional periodic (3DP) BC. This complexity can be improved by utilizing mesh-based Ewald-type methods leading to $\mathcal{O}(N \log N)$ scaling. Particle-Particle, Particle-Mesh(P^3M) and Particle Mesh Ewald(PME) are well-known Ewald-type mesh-based methods which both scale $\mathcal{O}(N \log N)$, and the P^3M method is said to be faster [16]. Ewald-type mesh-based methods are among the best methods (perhaps the best methods) for systems with 3DP BC. On the contrary these methods have not been successful in other types of BCs such as 2DP1DF BC, etc. Although 3DP BC methods have been extensively used for the other type of BCs by adding an empty region (gap) in the nonperiodic direction(s) or sometimes in addition to the gap by adding correction term(s) to the potential to decouple(compensate) the undesired interaction between images in the nonperiodic direction(s). Unfortunately the imposition of artificial periodicity, which is naturally added by Ewald-type methods in the wake of using Discrete Fourier Transform, may lead to artifacts, e.g. in implicit solvent systems [18, 19]. A discussion of Ewald-type methods, with further references can be found in Ref. [20].

Cutoff Methods These methods neglect the long range nature of the Coulomb potential and, by this assumption, the sum over the Coulomb potential function is elaborately truncated. This leads to a computationally favorable $\mathcal{O}(N)$ scaling as well as high capability of parallelization. One can readily apply these methods to different types of BCs. Unfortunately the use of cutoff methods, however, has been shown to introduce significant errors and artifacts in simulations [21, 22, 23, 24, 25, 26]. Truncation of the Coulomb potential is held responsible for the poor reproduction of, for instance, dielectric properties or radial distribution function [27, 28, 29, 30]. For a detailed investigation on this subject, see the references in Ref. [31].

Convergence Factor Approaches In these methods, the Coulomb potential function is modified to a new function which depends on a new parameter such that this function converges to the Coulomb potential function as the new parameter goes to a certain value, say zero. Lekner [32] developed a method based on a convergence factor which efficiently sums up the Coulomb potential for a system with 3D periodic BC. Later Sperb and co-workers [33] developed a method named MMM, competitive

to FFT mesh-based Ewald-type methods for high accuracy. This method leads to complexity of $\mathcal{O}(N \log N)$. In 2002, Arnold et al introduced a variation of MMM satisfying 2DP1DF BC, called MMM2D [46] which scales $\mathcal{O}(N^{\frac{5}{3}})$. And they also developed MMM1D [53] for BC with periodicity in only one direction which scales $\mathcal{O}(N^2)$. The outstanding advantage of these methods is that they offer an “*a priori*” error estimate which is a user-friendly feature. Unfortunately they all are superior to the other methods only for the high accuracy evaluation of the Coulomb interaction that it is usually not required.

Hierarchical or Multipole Methods Multipole methods, which mainly consist of two types, i.e. Fast Multipole Methods(FMM) and Tree-Codes methods, are based on the observation that distant charges may be grouped together and substitute by a single multipole expansion, leading to a substantial saving in the number of interaction terms necessary to sum the potential or the forces. Since the multipole expansion is calculated in real space, the periodicity only enters through the expansion coefficients. Therefore multipole methods are not restricted to an especial kind of BC. Despite the fact that the fast multipole methods scale linearly, these methods become competitive to the other methods only for particle numbers above 10^6 . The exact value depends on the particular BC and the required accuracy.

Methods for calculating long range Coulomb interaction have been compared in Refs. [14, 15, 16, 17]. In this chapter I present two novel methods which calculate the Coulomb interaction efficiently and accurately, one for 3DF BC named Particle-Particle, Particle-Scaling (P^3S) and the other for 2DP1DF BC named Particle-Particle, Particle-Density (P^3D). These two methods intrinsically satisfy their corresponding BCs. Furthermore, they have been implemented and tested successfully. I also show results obtained by these two methods in this chapter.

2.1 Particle-Particle, Particle-Scaling Method

In this section we present our novel method to calculate Coulomb interaction for the 3DF BC. The total electrostatic energy of N point charges in the 3DF BC is given by

$$E = \frac{1}{2} \sum_{\substack{i,j=1 \\ i \neq j}}^N \frac{q_i q_j}{|\mathbf{r}_i - \mathbf{r}_j|}$$

As in the Ewald-type methods by adding and subtracting the terms corresponding to the electrostatic energy of collection of smooth charge densities $\rho_i(\mathbf{r})$, centered at the particle

positions \mathbf{r}_i , we get

$$E = \frac{1}{2} \sum_{\substack{i,j=1 \\ i \neq j}}^N \left[\frac{q_i q_j}{|\mathbf{r}_i - \mathbf{r}_j|} - \int \int \frac{\rho_i(\mathbf{r}) \rho_j(\mathbf{r}')}{|\mathbf{r} - \mathbf{r}'|} d\mathbf{r} d\mathbf{r}' \right] + \frac{1}{2} \sum_{i,j=1}^N \int \int \frac{\rho_i(\mathbf{r}) \rho_j(\mathbf{r}')}{|\mathbf{r} - \mathbf{r}'|} d\mathbf{r} d\mathbf{r}' - \frac{1}{2} \sum_{i=1}^N \int \int \frac{\rho_i(\mathbf{r}) \rho_i(\mathbf{r}')}{|\mathbf{r} - \mathbf{r}'|} d\mathbf{r} d\mathbf{r}'. \quad (2.1)$$

Choosing $\rho_i(\mathbf{r})$ to be Gaussian has several advantages from the numerical viewpoint.

$$\rho_i(\mathbf{r}) = \frac{q_i}{(\alpha^2 \pi)^{\frac{3}{2}}} \exp \left[-\frac{|\mathbf{r} - \mathbf{r}_i|^2}{\alpha^2} \right] \quad (2.2)$$

Using the above smooth charge density yields

$$E = \frac{1}{2} \sum_{\substack{i,j=1 \\ i \neq j}}^N \frac{q_i q_j \operatorname{erfc} \left[\frac{|\mathbf{r}_i - \mathbf{r}_j|}{\alpha \sqrt{2}} \right]}{|\mathbf{r}_i - \mathbf{r}_j|} + \frac{1}{2} \sum_{i,j=1}^N \int \int \frac{\rho_i(\mathbf{r}) \rho_j(\mathbf{r}')}{|\mathbf{r} - \mathbf{r}'|} d\mathbf{r} d\mathbf{r}' - \frac{1}{\alpha \sqrt{2\pi}} \sum_{i=1}^N q_i^2 \quad (2.3)$$

The calculation of the third term is trivial. The calculation of the first term which in fact is short range can be performed $\mathcal{O}(N)$, if one utilizes a modified linked cell list as explained in Ref. [34]. The calculation of the long range part in the Eq. (2.3), the second term, is the main challenge in Ewald-type methods. In our new method we calculate the long range energy using interpolating scaling functions. Unlike the calculation in Fourier space, there is no imposition of periodic BC on the system while expanding the smooth charge density in terms of interpolating scaling function.

$$\rho(\mathbf{r}) \approx \tilde{\rho}(\mathbf{r}) = \sum_{\mathbf{i}} \rho_{\mathbf{i}} \phi_{\mathbf{i}}(\mathbf{r}), \quad \mathbf{i} := (i_1, i_2, i_3) \quad (2.4)$$

$$\phi_{\mathbf{i}}(\mathbf{r}) = \phi(x/h - i_1) \phi(y/h - i_2) \phi(z/h - i_3) \quad (2.5)$$

It was suggested in Ref. [35] to take the interpolating scaling functions [36] of high order (up to 100) as the basis functions $\phi(x)$. The scaling function of order N interpolates the polynomials of order N exactly and is reasonably localized. Therefore, it can interpolate a Gaussian very well. On the other hand, since the interpolating scaling functions form a cardinal¹ basis set corresponding to an equidistantly spaced grid, the coefficients in Eq. (2.4) are obtained by

$$\rho_{\mathbf{i}} = \rho(\mathbf{i}h) \quad (2.6)$$

¹A simple explanation of cardinal basis set is as following: assuming a set of functions corresponding to a grid, each function has zero value at all grid points except one particular grid point which that function belongs to.

The potential that arises from the approximate charge distribution $\tilde{\rho}(\mathbf{r})$ is given by

$$V(\mathbf{r}) = \int \frac{\tilde{\rho}(\mathbf{r}')}{|\mathbf{r} - \mathbf{r}'|} d\mathbf{r}' \quad (2.7)$$

At a grid point \mathbf{i} , this potential has the form

$$V_{\mathbf{i}} := V(\mathbf{i}h) = h^2 \sum_{\mathbf{j}} K_{\mathbf{j}-\mathbf{i}} \rho_{\mathbf{j}} \quad (2.8)$$

$$K_{\mathbf{j}} := \int \frac{\phi_{\mathbf{j}}(\mathbf{r})}{|\mathbf{r}|} d\mathbf{r} \quad (2.9)$$

K is the kernel calculated as in Ref. [35]. The long range energy is calculated as,

$$E_{long} \approx \frac{h^3}{2} \sum_{\mathbf{i}} \rho_{\mathbf{i}} V_{\mathbf{i}} = \frac{h^5}{2} \sum_{\mathbf{ij}} \rho_{\mathbf{i}} \rho_{\mathbf{j}} K_{\mathbf{i}-\mathbf{j}} \quad (2.10)$$

The latter sum is a convolution that can be calculated via FFT techniques. The energy is a product of FFT transform of $\rho_{\mathbf{i}}$ squared times the FFT transform of $K_{\mathbf{i}}$, times a constant. The kernel is calculated only once at the beginning of a calculation. Thus after the kernel is calculated, FFT routines are needed to calculate the energy and it also follows that the use of high order interpolating scaling functions only increases the calculation time of the kernel not the calculation time of the potential energy and the forces.

2.2 The Results of the P^3S Method

To evaluate the accuracy and the performance of the P^3S method we have applied it to a test system of N particles with charges ± 1 with coordinates moved randomly from a rock salt crystalline position. In Fig. 2.1, the CPU time versus relative mean square (MSQ) force error, for different number of atoms, obtained from the Pareto frontiers optimization is given for the test system. A point is on the Pareto frontier if there is no other point which has both smaller CPU time and a smaller ratio of the rms force error to the norm of forces,

$$\sqrt{\frac{\sum_{i=1}^N (\mathbf{F}_i - \mathbf{F}_i^{exact})^2}{\sum_{i=1}^N (\mathbf{F}_i^{exact})^2}}, \quad (2.11)$$

It can be seen from Fig. 2.1 that high accuracy can be achieved for various number of atoms. In contrast to the other methods such as the Fast Multiple Method, the P^3S method has the following advantage, which is of importance both in molecular dynamics simulations and minimization schemes: the approximate energy is conserved, in other words the approximate forces are the exact analytical derivative of the approximate energy. This ensures energy conservation during an MD run. To illustrate this, we made an MD simulation of a rock salt crystal formed by 1000 Na and Cl atoms. The particle positions and velocities are updated by the velocity Verlet algorithm. To get physically reasonable results, we made the particles interact through the Born-Mayer-Huggins-Fumi-Tosi (BMHFT) rigid-ion potential[37] that has bonding terms in addition to the Coulombic force. At first we let the system equilibrate for 300 oscillation periods. We then monitored the potential and the total energy for another 100 periods using the exact direct all-pair summation algorithm. Then the last 100 periods were repeated using our P3S algorithm. On Figs. 2.2 and 2.3, the absolute values of deviations of the potential and the total energy from their mean values are plotted. The ratio of the mean square deviation of the total energy to that of the potential one is found to be 1.4×10^{-3} .

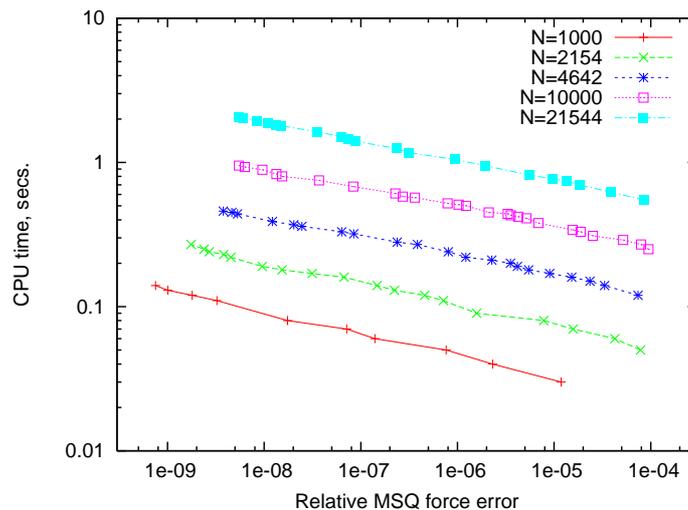


Figure 2.1: The Pareto frontiers for the crystal system.

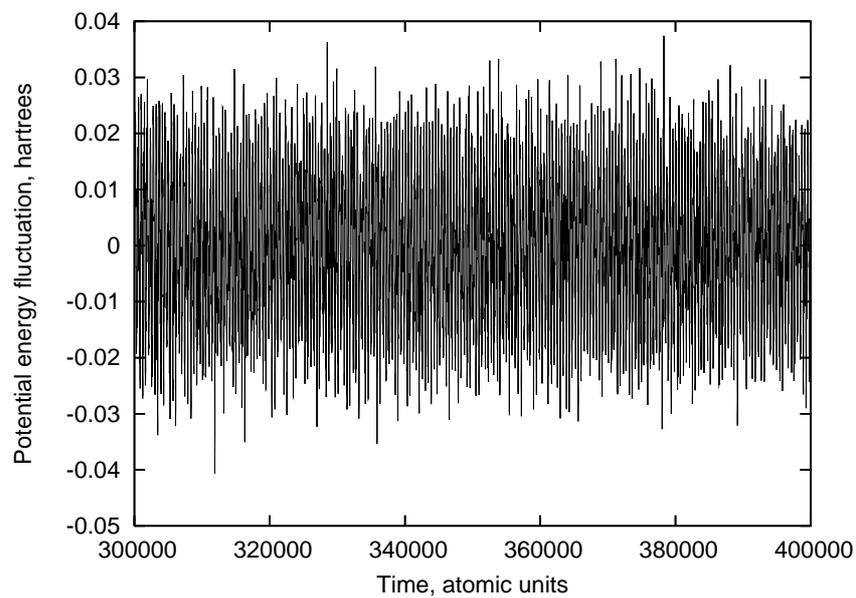


Figure 2.2: The potential energy fluctuations with the P3S method.

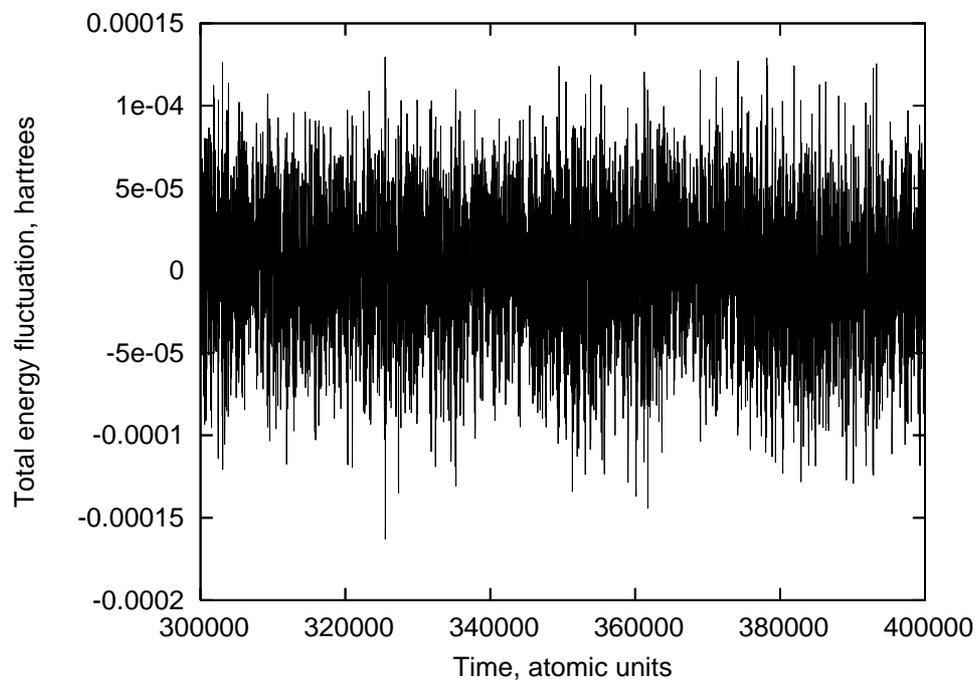


Figure 2.3: The total energy fluctuations with the P3S method.

2.3 Particle-Particle, Particle-Density Method

Simulations of systems with slab-like geometries are of great importance. Problems involving surfaces, interfaces, tip-surface interaction in scanning probe microscopy simulations, electrolytes trapped between two plates, thin films of ferrofluids, etc. all fall into this category. Calculating the Coulomb interaction in such settings is a major challenge. With free boundary conditions (i.e. the potential tends to zero at infinity) the scaling of the trivial direct summation is $\mathcal{O}(N^2)$ where N is the number of particles. In the case of 2D periodic and 1D free (2DP1DF) boundary conditions (BC) the situation is even worse. In principle one would then have to include into the summation the interactions with all the periodic images in the two periodic directions.

Algorithms such as Ewald-based methods [38], fast multipole methods (FMM)[39], P³M method[40], and convergence factor approaches[32, 41, 33] have therefore been generalized to 2DP1DF problems. Handling different types of BC in the FMM[42] is straightforward. In addition FMM methods have the ideal linear scaling. Unfortunately the prefactors in FFM methods are typically large and so FMM methods are in many cases only faster than the other methods for $N > 10^6$, where N is the number of particles. Another drawback of FMM that is important in molecular dynamics is that the approximate FMM forces are not exact analytical derivatives of the approximate energy. For example, in a molecular dynamics simulation in which FMM is used to calculate the electrostatic energy, a discontinuity occurs whenever an atom crosses cell boundaries. Therefore the energy is not conserved during the molecular dynamics simulation. Highly accurate energy conservation is therefore impossible to achieve.

Ewald methods for the 2DP1DF boundary conditions, called EW2D, have been developed Refs. [43, 44, 45]. A comparison of three versions of the EW2D methods can be found in Ref. [15]. Unfortunately, the practical use of the EW2D sum is hampered by the occurrence of a reciprocal space term. The resulting Fourier space sum does not allow for a product decomposition as it is done in the 3DP Ewald methods and therefore the method has a scaling of $\mathcal{O}(N^2)$. In 2002 Arnold and Holm developed MMM2D[46] (MMM with 2DP1DF BC), which is found to be the best in terms of accuracy. Another advantage of this method is that it has “*a priori*” error estimates. However, because of its $\mathcal{O}(N^{\frac{5}{3}})$ scaling it is only suitable for a small number of atoms.

A rather simple approach is to use the standard 3DP Ewald method (EW3D) also for 2DP1DF boundary conditions. Spohr showed that the regular EW3D method almost reproduces the EW2D results[47], provided that the box length in the non-periodic direction is about five times larger than those in the periodic directions, i.e. that there is empty space of sufficient thickness in the basic periodic box to dampen out the inter-slab interactions. There are also methods with correction terms to make the 3D periodical scheme applicable to the 2DP1DF systems and resolve the problem of slow convergence with respect to the thickness, so that a medium size gap(empty space) is enough. The

EW3DC[48, 49] method consists of a modification of EW3D to account for the slab geometry and addition of a correction term to remove the forces due to the net dipole of the periodically repeated slabs. Methods with layer correction terms to eliminate the inter-slab interaction, in addition to the correction term responsible for net dipole, have been mixed with the mesh-based methods, thus achieving almost linear scaling e.g. EW3DLC[50, 51], P³MLC[50, 51]. The main drawback of these methods is that the errors in the forces on the particles near to the surfaces are larger than in the middle. Although the error becomes negligible by choosing proper values for the empty space[52], this reduces the efficiency of the method. An interesting feature of EW3DLC is that there is an “*a priori*” error estimate for the layer correction term.

In this section I present a method which fills the gap of absence of an efficient method for medium size systems having $10^2 - 10^6$ particles. Because our method is not based on a modification of a fully periodic method, no replication is needed in the non-periodic direction, leading to smaller memory and CPU requirements. In contrast to some others, our method does not impose any restriction on the distribution of particles in the non-periodic direction.

2.3.1 Coulomb interaction for systems with periodic boundary conditions in two dimensions and free in the other one

Despite the fact that the calculation of the Coulomb interaction with 2DP1DF BC is of great importance due to its numerous applications in the surface science, there are not many successful methods to handle such problems and three dimensional periodic methods have been mostly used by including an empty space in the nonperiodic direction together with appropriate correction terms. In this section I present a novel method which intrinsically preserves 2DP1DF BC and scales $N \log N$, in addition, the error in forces is uniformly distributed through out the simulation box. Although we have not parallelized our code yet, the parallelizability of this method would have similar limitations as other FFT based methods.

Consider a system of N particles with charges q_i at positions \mathbf{r}_i in an overall neutral and rectangular simulation box of dimensions L_x, L_y and L_z . The Coulomb potential energy of this system with periodic boundary condition in two directions and free boundary condition in the third direction (let us say in the z direction) can be written as

$$E = \frac{1}{2} \sum_{\mathbf{n}}' \sum_{i,j=1}^N \frac{q_i q_j}{|\mathbf{r}_{ij} + \mathbf{n}|} \quad (2.12)$$

where $\mathbf{r}_{ij} = \mathbf{r}_i - \mathbf{r}_j$ and $\mathbf{n} = (n_x L_x, n_y L_y, 0)$, with n_x, n_y being integers. The prime on the outer sum denotes that for $\mathbf{n} = 0$ the term $i = j$ has to be omitted.

In the Ewald-type methods the above very slowly converging sum over the Coulomb potential function is split into two sums which converge exponentially fast, one in the real space and the other in the Fourier space. This splitting can be done by adding and subtracting a term corresponding to the electrostatic energy of a system of smooth spherical charge densities, $\rho_i(\mathbf{r})$, centered on the particle positions:

$$\begin{aligned}
E &= \frac{1}{2} \sum_{\mathbf{n}}' \sum_{i,j=1}^N \left[\frac{q_i q_j}{|\mathbf{r}_{ij} + \mathbf{n}|} - \iint \frac{\rho_i(\mathbf{r}) \rho_j(\mathbf{r}' + \mathbf{n})}{|\mathbf{r} - \mathbf{r}'|} d\mathbf{r} d\mathbf{r}' \right] \\
&+ \frac{1}{2} \sum_{\mathbf{n}} \sum_{i,j=1}^N \iint \frac{\rho_i(\mathbf{r}) \rho_j(\mathbf{r}' + \mathbf{n})}{|\mathbf{r} - \mathbf{r}'|} d\mathbf{r} d\mathbf{r}' \\
&- \frac{1}{2} \sum_{i=1}^N \iint \frac{\rho_i(\mathbf{r}) \rho_i(\mathbf{r}')}{|\mathbf{r} - \mathbf{r}'|} d\mathbf{r} d\mathbf{r}' \tag{2.13}
\end{aligned}$$

The aim of the last term is to subtract the self energy for $\mathbf{n} = 0$ and $i = j$ which is included in the second term.

Even though Ewald-type methods allow for any choice of $\rho_i(r)$, it was noted in Refs. [16, 34] that Gaussians are virtually optimal in practice. By choosing $\rho_i(r)$ to be a Gaussian function

$$\rho_i(\mathbf{r}) = \frac{q_i}{(\alpha^2 \pi)^{\frac{3}{2}}} \exp \left[-\frac{|\mathbf{r} - \mathbf{r}_i|^2}{\alpha^2} \right] \tag{2.14}$$

the first and the third terms in the Eq. (2.13) can be rewritten as follows [16]:

$$\begin{aligned}
E &= \frac{1}{2} \sum_{\mathbf{n}}' \sum_{i,j=1}^N \frac{q_i q_j \operatorname{erfc} \left[\frac{|\mathbf{r}_{ij} + \mathbf{n}|}{\alpha \sqrt{2}} \right]}{|\mathbf{r}_{ij} + \mathbf{n}|} + \\
&+ \frac{1}{2} \sum_{\mathbf{n}} \sum_{i,j=1}^N \iint \frac{\rho_i(\mathbf{r}) \rho_j(\mathbf{r}' + \mathbf{n})}{|\mathbf{r} - \mathbf{r}'|} d\mathbf{r} d\mathbf{r}' \\
&- \frac{1}{\alpha \sqrt{2\pi}} \sum_{i=1}^N q_i^2 \tag{2.15}
\end{aligned}$$

Obviously, the calculation of the third term is trivial. Since the interaction in the first term is decaying exponentially it can be made of finite range by introducing a cut-off. The error resulting from the cut-off is then also exponentially small and the short range term can be calculated with linear scaling. We have calculated the short range part and also the contribution of the forces from the long range part as described in Ref. [34].

The major difficulty is the calculation of the second term. A method to solve the Poisson's equation under 2DP1DF boundary conditions has recently been put forward by L. Genovese and coworkers [54]. Our approach is similar. As in Ref. [54] we use plane waves [55]

to represent the charge density in the periodic directions. Whereas Genovese et al used scaling functions as the basis in the non-periodic direction, we use finite elements for that purpose. Scaling functions are presumably the optimal choice in the context of electronic structure calculations where the charge density is given on a numerical grid. In our case the charge distribution is a sum over smooth Gaussians that can easily be represented by our mixed basis set of plane waves and finite elements. As will be seen we can avoid storing any kernel if we solve a differential equation along the z -axis instead of solving an integral equation. We use a family of finite elements that allows to solve the linear system of equations resulting from the differential equation very efficiently.

2.3.2 Calculating the long range part

The second term in Eq. (2.15), can be written as

$$E_{long} = \frac{1}{2} \int_{\mathbb{R}^3} \rho^{(N)}(\mathbf{r}) V(\mathbf{r}) d\mathbf{r} \quad (2.16)$$

where

$$\rho^{(N)}(\mathbf{r}) := \sum_{i=1}^N \rho_i(\mathbf{r}) \quad (2.17a)$$

$$V(\mathbf{r}) := \int_{\mathbb{R}^3} \frac{\rho(\mathbf{r}')}{|\mathbf{r} - \mathbf{r}'|} d\mathbf{r}' \quad (2.17b)$$

$$\rho(\mathbf{r}) := \sum_{\mathbf{n}} \sum_{j=1}^N \rho_j(\mathbf{r} + \mathbf{n}) \quad (2.17c)$$

We consider a system with a charge density that is only localized in the non-periodic direction, in our notation z ; $\rho(x, y, z) = 0 \forall (x, y, z) \in \mathbb{R}^3 \mid z \notin [z_l, z_u]$. We define the cell containing the continuous charge density as:

$$\mathcal{V} := [0, L_x] \otimes [0, L_y] \otimes [z_l, z_u]$$

In our case the length of \mathcal{V} in z direction $z_u - z_l$ is L_z plus twice the cut-off for Gaussians. Since $\rho(\mathbf{r})$ is periodic in x and y direction, $V(\mathbf{r})$ is periodic too, so we can rewrite Eq. (2.16) as:

$$E_{long} = \frac{1}{2} \int_{\mathcal{V}} \rho(\mathbf{r}) V(\mathbf{r}) d\mathbf{r} \quad (2.18)$$

and $V(\mathbf{r})$ can be calculated in an alternative way to Eq. (2.17b). It can be considered as the solution of Poisson's equation with 2DP1DF BC:

$$\nabla^2 V(\mathbf{r}) = -4\pi\rho(\mathbf{r}) \quad (2.19)$$

In order to calculate the contribution of the forces resulting from the long range part, the following equation is used.

$$\mathbf{F}_i^{(long)} = \frac{1}{2} \int_{\mathcal{V}} \zeta_i(\mathbf{r}) V(\mathbf{r}) d\mathbf{r} \approx \frac{1}{2} \sum_{klm} \zeta_{klm}^{(i)} V_{klm} \quad (2.20)$$

where $\zeta_i(\mathbf{r})$ is the gradient of Gaussian charge distribution with respect to particle position \mathbf{r}_i , more details can be found in Ref. [34]. The charge density and the potential are periodic in x and y directions. Hence we can write the potential and the charge density in terms of Fourier series:

$$V(x, y, z) = \sum_{k, l=-\infty}^{\infty} c_{kl}(z) \exp \left[2i\pi \left(\frac{kx}{L_x} + \frac{ly}{L_y} \right) \right] \quad (2.21a)$$

$$\rho(x, y, z) = \sum_{k, l=-\infty}^{\infty} \frac{\eta_{kl}(z)}{-4\pi} \exp \left[2i\pi \left(\frac{kx}{L_x} + \frac{ly}{L_y} \right) \right] \quad (2.21b)$$

Inserting Eqs. (2.21a) and (2.21b) in Eq. (2.19) yields:

$$\left(\frac{d^2}{dz^2} - g_{kl}^2 \right) c_{kl}(z) = \eta_{kl}(z) \quad (2.22)$$

$$g_{kl} := 2\pi \sqrt{\frac{k^2}{L_x^2} + \frac{l^2}{L_y^2}}$$

$$\begin{aligned} \eta_{kl}(z) = & \frac{-4\pi}{L_x L_y} \int_0^{L_x} \int_0^{L_y} \rho(x, y, z) \\ & \times \exp \left[-2i\pi \left(\frac{kx}{L_x} + \frac{ly}{L_y} \right) \right] dx dy \end{aligned} \quad (2.23)$$

To solve the differential equation (2.22) one needs to have boundary conditions at $z \rightarrow \pm\infty$ for $c_{kl}(z)$. The potential obtained by solving Poisson's equation should be the same as the one in Eq. (2.17b). Hence we derive the boundary condition in the non-periodic direction from Eq. (2.17b). Considering the fact that the charge density is supposed to be limited in the non-periodic direction. We search for the boundary condition at $z \rightarrow \pm\infty$ yields $|\mathbf{r} - \mathbf{r}'| \neq \mathbf{0}$. By performing the Taylor expansion of $\frac{1}{|\mathbf{r} - \mathbf{r}'|}$ about $z' = 0$ in the integral expression of Eq. (2.17b) for the exact potential $V(x, y, z)$ arising from our periodic charge distribution $\rho(\mathbf{r})$

$$\begin{aligned} V(x, y, z) = & \int_{z_l}^{z_u} \int_{-\infty}^{\infty} \int_{-\infty}^{\infty} dx' dy' dz' \frac{1}{|\mathbf{r} - \mathbf{r}'|} \\ & \times \sum_{k, l=-\infty}^{\infty} \frac{\eta_{kl}(z')}{-4\pi} \exp \left[2\pi i \left(\frac{kx'}{L_x} + \frac{ly'}{L_y} \right) \right] \end{aligned} \quad (2.24)$$

one can show that $V(x, y, z \rightarrow \pm\infty) = \mp\beta$ where β is proportional to the dipole moment of the charge distribution along the z direction

$$\beta = \frac{1}{2} \int_{z_l}^{z_u} \eta_{00}(z') z' dz' \quad (2.25)$$

For the Gaussian charge distributions given by Eq. (2.14) the above integral can be calculated analytically and β is calculated exactly.

$$\beta = \frac{-2\pi}{L_x L_y} \sum_{i=1}^N q_i z_i \quad (2.26)$$

This boundary condition for the potential gives the following conditions for the g 's.

- $g = g_{00} = 0 \Rightarrow \frac{d^2}{dz^2} c_{00}(z) = \eta_{00}(z)$ We solve this differential equation with boundary condition $c_{00}(z \rightarrow \pm\infty) = \mp\beta$
- $g = g_{kl} \neq 0 \Rightarrow \left(\frac{d^2}{dz^2} - g_{kl}^2 \right) c_{kl}(z) = \eta_{kl}(z)$ For all of these differential equations we have to impose BC of the form $c_{kl}(z \rightarrow \pm\infty) = 0$.

The solution for $c_{00}(z)$ is a linear function outside the interval $[z_l, z_u]$. Since the boundary conditions are applied at infinity the linear term has to vanish and one has to satisfy Dirichlet BC for c_{00} , namely $c_{00}(z_u) = -\beta$ and $c_{00}(z_l) = \beta$. For $|k| + |l| > 0$, $c_{kl}(z)$ will have Robin BC as explained below. The potential is thus not modified if one takes for instance a computational box that is thicker in the z direction than necessary. The thinnest possible box is the one that just includes the region where the charge is nonzero.

For $z \in (-\infty, z_l]$ we have $\eta_{kl}(z) = 0$, thus

$$c(z) = c(z_l) e^{g_{kl}(z-z_l)} \quad (2.27)$$

Both $c(z)$ and its derivative must be continuous. So performing left differentiation at z_l we get:

$$c'(z_l) - g_{kl} c(z_l) = 0 \quad (2.28)$$

With a similar procedure we obtain the BC at z_u :

$$c'(z_u) + g_{kl} c(z_u) = 0 \quad (2.29)$$

These BCs are in agreement with the BCs resulting from the Green functions in Ref. [54].

2.3.3 Solving the ordinary differential equation using the finite element method

We recapitulate the procedure of solving the differential equation for the case $|k| + |l| > 0$, i.e. $g_{kl} \neq 0$, using the finite element method. For the case $k = l = 0$ the approach is similar, with the only difference that the Dirichlet BC are used. The case $k = l = 0$ can be found in many manuscripts and textbooks on the finite element method e.g. Ref. [56]. In particular our notation follows Ref. [56]. Discretizing the differential equation with the mentioned Robin BCs using the finite element method leads to a system of linear equations. The resulting matrix is a banded matrix for which the system of equations can be solved efficiently if high-order hierarchical piecewise polynomials are used as a basis and if the degrees of freedom are decimated. More precisely, we expand the function in terms of linear functions as well as high-order polynomials, but we do not calculate the expansion coefficients of the high-order polynomials. To do this, the original system of equations is modified to decimate the degrees of freedom only to those of associated with the linear basis functions. This procedure leads to a linear system of equations with tridiagonal matrix. The employed hierarchical finite element basis set leads to algebraic systems that are less susceptible to round-off error accumulation at high order than those produced by a Lagrange basis [57]. We use linear hat functions as the linear hierarchical basis. For higher order bases we exploit the method of Szabó and Babuška [58] which relies on Legendre polynomials. In Appendix A we discuss in detail the expansion of $c(z)$ in terms of the hat functions and the higher order hierarchical piecewise polynomials on the interval $[z_{i-1}, z_i]$:

$$c(z) \approx c_{i-1}N_{-1}(\xi_i) + c_iN_1(\xi_i) + \sum_{j=2}^p c_{i,j}N_j(\xi_i), \quad (2.30)$$

where $\xi_i = 2(z - z_i)/h + 1$; $h = z_i - z_{i-1}$ and the functions $N_i(\xi)$ in the interval $[-1, 1]$ are given by

$$N_{-1}(\xi) = \frac{1 - \xi}{2} \quad N_1(\xi) = \frac{1 + \xi}{2} \quad (2.31a)$$

$$N_i(\xi) = \sqrt{\frac{2i-1}{2}} \int_{-1}^{\xi} P_{i-1}(\xi') d\xi', \quad i \geq 2 \quad (2.31b)$$

where $P_i(\xi)$ are Legendre polynomials. These hierarchical bases have useful orthogonal properties that lead to sparse and well-conditioned stiffness matrices. Defining the operator \mathcal{L}

$$\mathcal{L}[c] := c''(z) - g^2c(z) \quad (2.32)$$

we can write our differential equation (2.22) as

$$\mathcal{L}[c] = \eta(z)$$

with boundary conditions

$$\begin{cases} c'(z_l) - gc(z_l) = 0 \\ c'(z_u) + gc(z_u) = 0 \end{cases} \quad (2.33)$$

The method of weighted residuals is used to construct a variational integral formulation of Eq. (2.32) by multiplying with a test function $d(z)$ and integrating over $[z_l, z_u]$:

$$(d, \mathcal{L}[c] - \eta) = 0 \quad \forall d \in H^1(z_l, z_u) \quad (2.34)$$

where H^1 is the Sobolev space. Sobolev spaces are sets of functions which all have a certain degree of smoothness. We have introduced the L^2 inner product

$$(d, c) := \int_{z_l}^{z_u} d(z)c(z)dz \quad (2.35)$$

Performing the integration by parts in Eq. (2.34) and applying Robin BCs given in Eq. (2.33) gives

$$A(d, c) = (d, \eta) + gd(z_l)c(z_l) + gd(z_u)c(z_u) \quad (2.36)$$

where

$$A(d, c) := \int_{z_l}^{z_u} [-d'(z)c'(z) - g^2d(z)c(z)] dz \quad (2.37)$$

Using the Galerkin approach and exploiting the decimation scheme, we can construct a system of linear equations $B\vec{c} = \vec{b}$ where the elements of the vector \vec{c} are the values of $c(z)$ at grid points. The detailed structure of this linear system of equations is given in the Appendix A.

In practice we put the charge density, the collection of the Gaussian charge distributions, on a uniform mesh $n_x \times n_y \times n_z$ and by performing n_z two-dimensional FFT we obtain $\eta_{kl}(z)$ on the grid points. The calculation time of this part scales as $n_x n_y n_z \log(n_x n_y)$, the inverse of this part, i.e. to calculate potential function from $c_{kl}(z)$ scales the same way. To calculate $c_{kl}(z)$ from $\eta_{kl}(z)$ we solve $n_x n_y$ systems of linear equations such that their corresponding matrix is tridiagonal. This part can be solved with a small prefactor and a complexity $\mathcal{O}(n_x n_y n_z)$. Thus the method scales overall as $N_g \log(N_g)$ where $N_g = n_x \times n_y \times n_z$.

2.4 Numerical Results

In this section we present numerical results obtained with our Poisson solver for continuous charge densities with 2DP1DF BC in stand alone mode and with our Ewald-like method for point particles interacting by Coulombic potential with 2DP1DF BC. We also show numerical evidence for the conservation of energy in a molecular dynamics simulation of a system composed of sodium chloride atoms.

2.4.1 Numerical results for the Poisson solver

Our method has an algebraic convergence rate in the non-periodic direction and a faster exponential convergence rate in the periodic directions, due to the finite element polynomial basis and to the plane wave representation, respectively. In Fig. 2.4 we show the convergence rate in the non-periodic direction with 7-th order finite elements ($p=7$ in Eq. (2.30)). For our test, the starting point was the potential rather than the charge density, since the charge density can be obtained analytically from the potential by simple differentiation. Our test potential had the form $V(\mathbf{r}) = \sin(a \sin(\frac{2\pi x}{L_x})) \sin(b \sin(\frac{2\pi y}{L_y})) \exp(-\frac{z^2}{c^2})$. This test potential has many frequencies in the periodic potential, thus it is a good potential for testing our implementation.

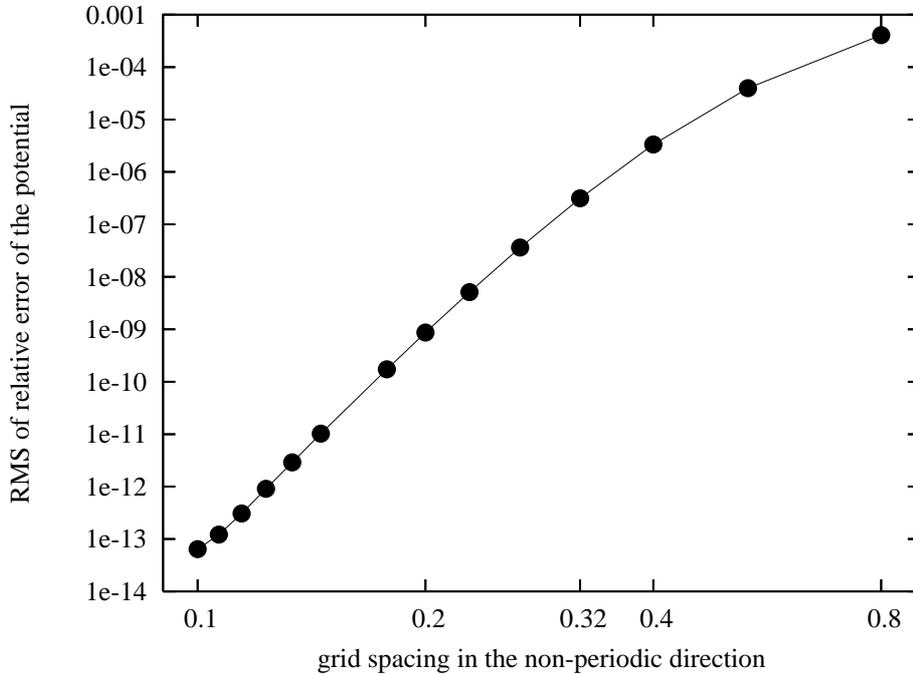


Figure 2.4: rms of relative error for the potential given in Sec. 2.4.1 with $a = 10, b = 10, c = 1, L_x = L_y = 1$. On this double logarithmic plot the curve has an asymptotic slope of 14 and machine precision can be reached.

2.4.2 Numerical results for point particles

In this section we give the numerical results of our implementation of the presented method for point particles. Since MMM2D is known to be highly accurate we use it as reference for comparison. First we want to demonstrate that errors along the non-periodic direction are uniformly distributed, unlike in 3D periodic methods with correction terms [49, 50, 51]. To this aim 100 particles were put randomly in a unit cubic cell and the program was run 100 times each time with different random positions. Results for the relative error of the forces exerted on each particle are plotted in Fig. 2.5.

In Fig. 2.6 we show that the theoretical scaling $\mathcal{O}(N \log(N))$ can be achieved in practice. The crossover with respect to MMM2D for a moderate accuracy of 10^{-4} in RMS relative error of the forces occurs for less than 20 particles. Both programs were run on an AMD Opteron 2400 MHz. The order of the finite elements is a parameter that can be optimized to obtain the smallest possible CPU time for a fixed accuracy. For high accuracies higher orders are recommended. The CPU time for the calculation of the forces dominates over the time needed to calculate the energy.

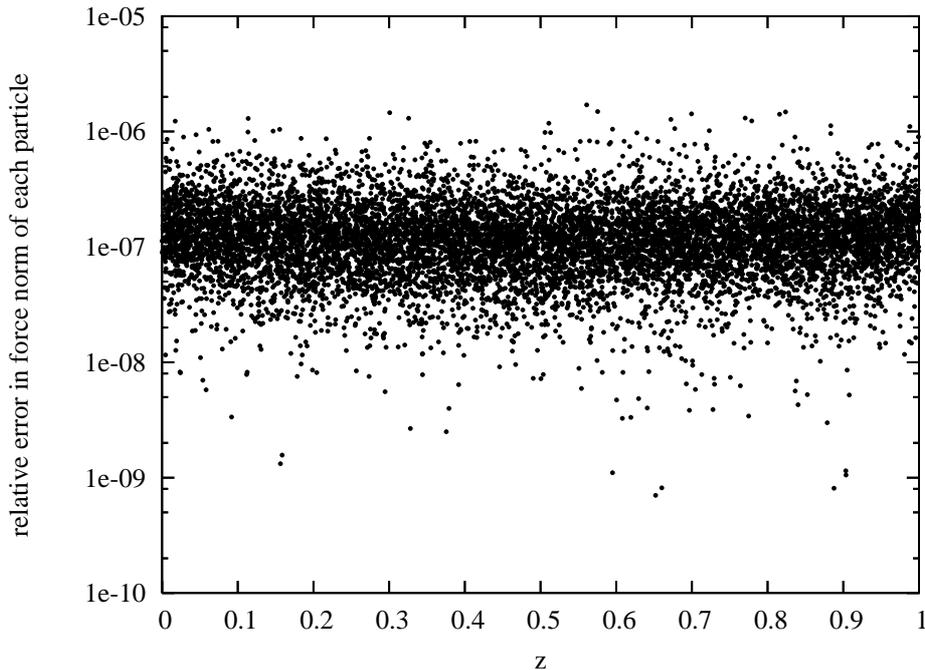


Figure 2.5: Relative error distribution of the force norm on each particle along the z-axis for 100 systems with 100 randomly distributed particles.

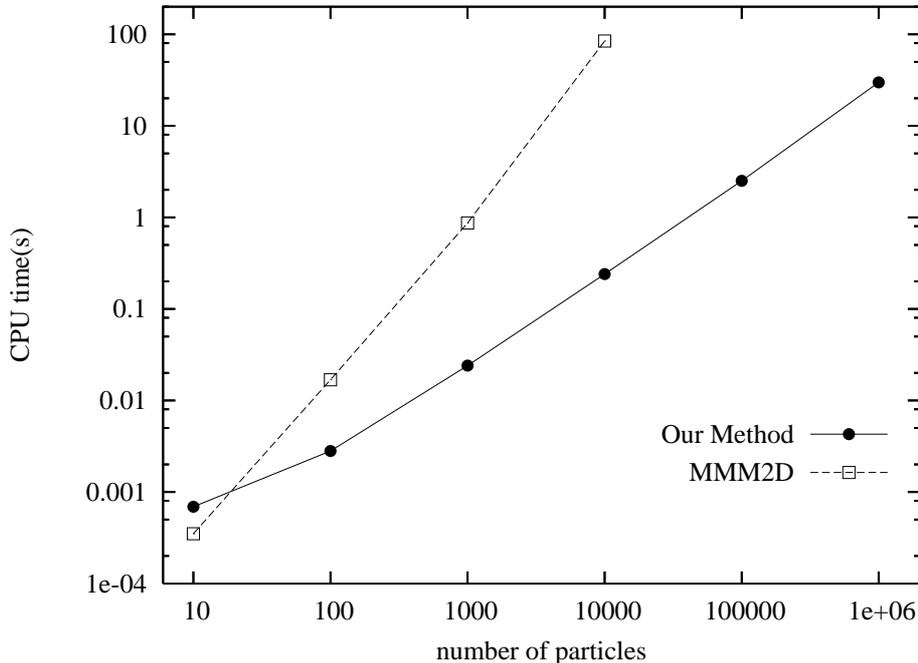


Figure 2.6: CPU time of one time evaluation of the forces on particles and the potential energy with our method (solid curve) and the MMM2D method (dashed curve).

2.4.3 Energy conservation

Ensuring energy conservation is of great importance in molecular dynamics simulations. In order to test energy conservation in a real simulation, we performed a very long (8 nano seconds) molecular dynamics simulation of a sodium chloride system containing 1000 particles. The velocity Verlet algorithm with a time step of 50 atomic units is used to update the particle positions and the velocities. The short range interactions were obtained from the Born-Mayer-Huggins-Fumi-Tosi (BMHFT) [37] rigid-ion potential, with the parameters of Ref. [59]. The shortest oscillation period was of the order of 3000 atomic units, i.e. 60 molecular dynamics steps. After equilibration for 1×10^6 steps, 7×10^6 steps were performed during which the total energy and potential energy were monitored. The fluctuation of the total energy, shown in Fig. 2.7, has an oscillation amplitude of about 2.5×10^{-5} , while the amplitude of the potential energy oscillation was 3 orders of magnitude larger. The total energy was conserved very well thus.

2.4.4 The optimal method parameters

Since the short range part is similar to the known Ewald-type methods, details concerning error resulting from cutting-off the summation in real space can be found in Ref. [60]. But handling the error resulting from the long range part is nontrivial because the long range

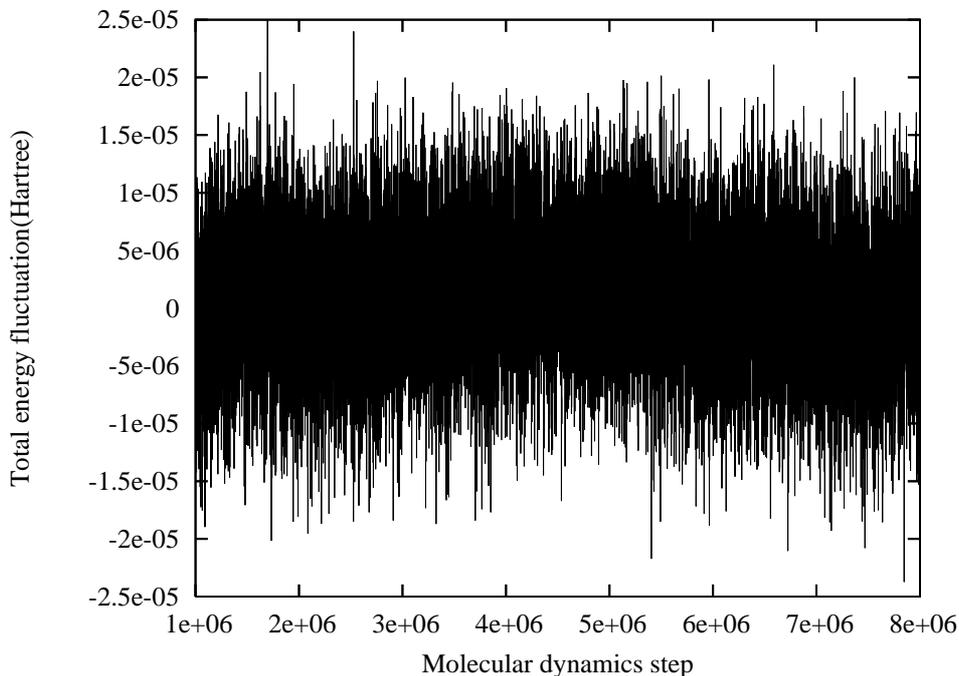


Figure 2.7: The total energy fluctuations calculated with our method.

part is solved by a method which is a mixture of plane wave and finite elements. In addition, the order of the polynomial for the finite elements, plays an important role in connection with both accuracy and efficiency. This fact makes the choice of the method parameters an intricate task. To overcome this problem, we performed a large number of runs for a Sodium Chloride crystalline system including 1000 atoms, each run with a different set of parameters. The optimal parameters were obtained from a Pareto frontier optimization.

In order to have an error estimate, we use the rms force error defined in Eq. 2.11 where \mathbf{F}_i^{exact} is approximated by \mathbf{F}_i obtained from the MMM2D method or our method with a set of parameters resulting to a very highly accurate forces and energy. All runs to determine the optimal method parameters were performed on a Intel(R) Pentium(R) 4 CPU 3.00GHz. A set of optimal method parameters for a wide range of preset accuracy are given in the Table 2.1. The parameter values given in Table 2.1 are optimal for the Sodium Chloride systems and also rough values for other rocksalt crystals. In fact, the parameters in Table 2.1 can be used for all alkali halide systems by scaling the parameters with the ratio of lattice constants. Test simulations are recommended for systems which have different crystalline structures.

Table 2.1: The optimal method parameters obtained by the Pareto frontier optimization. All parameters $h_{xy}, h_z, x_{max}, r_{cut}, \alpha$ are given in Angstrom while the bulk nearest-neighbor distance for Sodium Chloride is 2.8 Angstrom. The degree of the polynomial for the finite element is seven for all the runs.

rel. err. ^a	h_{xy} ^b	h_z ^c	x_{max} ^d	r_{cut} ^e	α ^f	time (s)
10^{-2}	1.55	2.33	4.0	5.00	2.10	0.012
10^{-3}	1.75	1.86	5.0	9.00	2.20	0.028
10^{-4}	1.55	1.64	7.0	10.0	2.10	0.040
10^{-5}	1.40	1.40	8.0	11.0	2.10	0.052
10^{-6}	1.27	1.33	7.5	12.0	2.20	0.068
10^{-7}	1.27	0.90	7.0	13.7	2.15	0.092
10^{-8}	1.07	0.70	7.9	13.7	2.10	0.120
10^{-9}	0.87	0.65	8.7	13.7	2.00	0.148
10^{-10}	0.93	0.56	8.7	14.0	1.95	0.172

^a ratio of rms force error to the norm of forces.

^b grid spacing in the periodic directions.

^c grid spacing in the nonperiodic direction.

^d cutoff radius of the Gaussian charge distribution.

^e cutoff radius of the real space term.

^f Ewald splitting parameter.

2.5 Conclusion

In this chapter I presented and validated two methods for calculating Coulomb interaction, one suitable for 3D isolated systems and the other for systems with a 2D slablike geometry. Both methods have several advantages of which two are common: *Both P^3S and P^3D methods intrinsically preserve the corresponding boundary conditions and they both can also achieve high precision.* It is shown that forces obtained by P^3S are analytical derivatives of the energy. Energy is thus conserved. The new P^3D method solves Poisson's equation for smooth charge densities with periodic boundary conditions in two directions and finite in the third one. The method is based on plane wave representation in the periodic directions and finite elements in the non-periodic direction. It is very efficient for smooth charge densities and does not require much memory. The resulting error distribution is uniform over the entire simulation cell. Based on this method we can calculate the electrostatic energy and forces on particles interacting by Coulombic potential with high accuracy and a $N \log(N)$ scaling. The method satisfies intrinsically and without any approximations the boundary conditions appropriate for surface problems. It is best suited for a moderate number of particles between $10^2 - 10^6$, and is expected to be suitable for an efficient parallelization since the time dominating parts are only loosely coupled.

Chapter 3

Candidates for Silicon Tip Structures

During the past few decades Scanning Probe Microscopy (SPM) and particularly Scanning Force Microscopy (SFM) have been used as powerful tools to investigate surface structures, nanotribology, etc., on a nano meter scale. An essential part of these tools is the tip. Even though considerable information about the macroscopic tip shape is known, so far little is known about the microscopic tip shape, namely tip-apex structure. In experiments, the macroscopic tip shape is determined by the tip preparation. It is thus controllable to some extent. On the other hand, the tip-apex atomic structure is *mainly* determined by the energy landscape of the tip-apex atoms. This means that the tip-apex structure may be uncontrollable during the experimental measurement times. The tip-apex atoms tend to relax into the nearest low energy state. Another factor which affects the tip-apex structure, as it is typically noted by experimentalists, is the change of the tip-apex structure due to the interaction of the tip-apex and the sample. This is also weakly controllable and it is somehow implicitly related to the energy landscape of the tip-apex atoms. The ability to image, manipulate and chemically identify single atoms on semiconductor surfaces is ultimately determined by the tip-apex structure and its composition. The short-range interaction between the tip-apex and the sample is responsible for the image atomic-scale contrast in noncontact Atomic Force Microscopy (nc-AFM). Thus understanding the tip-apex structure can help scientists to elucidate the details of the short range interaction. The experimental tip preparation is one of the most delicate steps. There are some *rules of thumb* which are more or less followed in most experiments. The tips, mostly made from silicon and exposing oxidized surfaces, are usually annealed and cleaned by ion sputtering. After this procedure, some tips can yield atomic resolution but more often several scans over a surface region are required to get atomic contrast. In some cases even a gentle indentation is needed. During the scan or the indentation process the tip can strongly interact with the sample producing a transfer of atoms between the surface and the apex. The tip-surface interaction can also modify the atomic structure of the tip, thus generating an atomic protrusion without any atom transfer between the tip and the surface. Experimental advances in Dynamic Force

Spectroscopy (DFS) have allowed to obtain a reproducible and accurate experimental determination of the tip-sample interaction as a fraction of distance first at low temperature and recently at room temperature [62, 63]. Thanks to this detailed description, recent investigations, for example Ref. [67], have shown that topographic images and dissipation signals are very sensitive to the tip-apex structure. In the process of searching for likely tip-apex structures of model tips, two aspects should be taken into account: (a) the intrinsic stability of atomically sharp tips, i.e. can these tips be a result of the sputtering and annealing processes and can they be stable over relevant measurement times; and (b) the sharpening and contamination processes due to the tip-surface interaction. Nowadays, such information is difficult to obtain from experiment alone, but atomistic simulations can provide detailed insight into the tip-apex structures and atomic relaxation processes induced by tip-sample interactions. However the problem is very complex: the paucity of experimental information leaves many variables unknown in a system presenting an intricate energy landscape. To tackle this problem we need efficient, fast but still accurate tools.

Silicon tips are widely used in SFM experiments, especially in dynamic mode of Atomic Force Microscopy (AFM). True AFM uses the force acting between a sharp tip-apex and surface atoms as a probe. In the case of silicon tips and silicon surfaces this force is due to the formation of chemical covalent bonding between the apex atom of the probe tip and the surface atoms [130]. Such a bond begins to form at a very proximate apex-surface distance ($< 5 \text{ \AA}$) [66, 68].

In Ref. [94], small Si model tips containing 7, 10, and 13 Si atoms were used to investigate atomic-scale sharpening of silicon tips in noncontact atomic force microscopy. In that work, a mechanism for the sharpening of an initially blunt tip, by means of an irreversible structural change, is illustrated. Three small model tips, denoted as H3, T4 and dimer-like, have been used extensively by Perez and coworkers for different goals, namely (i) explaining the dissipation in the dynamic force microscopy [67], these results can describe the dissipation mechanisms only qualitatively and merely the mechanisms which are not associated with the intricacy of the energy landscape, (ii) postulating that the covalent chemical bonding between a dangling bond at the tip apex and the nearest surface atom is responsible for atomic resolution [66, 68], (iii) the chemical identification of individual surface atoms [65].

These small tip-apexes provide a useful description of the tip-surface chemical interaction but many other important properties and observations need larger model tips to be explored. For example, DFS experiments over the Sn/Si(111)-($\sqrt{3} \times \sqrt{3}$) surface show significant variations of the shape of the short range (SR) force curves measured over the same (or similar) surface ad-atom with respect to the tips used [64, 65]. The variations indicate diverse elastic responses of the tip apexes under the applied forces. Simulations performed with the small tip apexes reproduce and explain the basic features of SR force curves. However, they do not show the larger varieties observed in experiments. This discrepancy is mostly due to the restricted size of the nanoasperities used in the simulations.

The atomic layers which constitute the last few nanometers of the tip (not included in the small tip apexes), besides determining the position of the last apex atoms, control the mechanical response of the tip to the applied force. Notice that these mechanical properties also play an important role in the atomic manipulations taking place in the repulsive regime [70].

The radius of commercial silicon tips ranges from approximately 10 nm to 150 nm. Even for the sharper tips there are of the order of 100,000 Si atoms in a hemisphere with radius of 10 nm. Fortunately as it is shown in Ref. [71], events in amorphous silicon are nearly localized, e.g. all events investigated in Ref. [71] 30 – 50 Si atoms are involved. Therefore it is not necessary to simulate very large systems, but large enough to allow likely events to occur during simulations and thus form structures which are realistic. In order to investigate realistic tips, one should perform simulations with much larger clusters. This is not feasible even with a rather fast method like tight-binding. The solution to this problem was to use larger clusters (tens to hundreds of Si atoms) than those considered so far but not much larger, and to fix atoms in the base of the tip in bulk positions. Si atoms at the surface of the base have dangling bonds, these dangling bonds are saturated by H atoms as previously done for small silicon model tips. The effect of saturation is discussed in Ref. [68]. We have started our simulations with pyramidal shaped clusters in which atoms in the base are terminated by H atoms. The Si atoms in the base as well as the H atoms are kept fixed.

The arguments presented above show that the tip-apex structure strongly affects all the processes to achieve atomic resolution in DFM experiments. The topographic images, the dissipation signal, the force spectroscopy curves and atomic manipulation depend strongly on the tip-apex structure. To understand in detail all these fundamental processes, a complete and detailed investigation of realistic tip-apex structures is required i.e., studying their stability and the optimal atomic configurations of the apexes.

In this chapter we present a detailed and systematic study of the most likely structures that can be expected at the tip-apex of Si tips used in DFM experiments. To this aim we performed extensive large-scale simulations, using recently developed algorithms and techniques such as the Lenosky Si-H tight-binding (TB) scheme and the minima hopping method (MHM). The latter is a systematic method recently developed by S. Goedecker for finding the global minimum as well as low-lying minima of the potential energy surface (PES) of a many body system. Previous simulations of a similar kind [72] had only limited success because such an efficient minima search method was not available at the time.

3.1 Si-H Tight-Binding Scheme

To investigate the PES of large Si clusters, one needs to have an accurate and reasonably fast method describing or the Si-Si, Si-H and H-H interactions. Ab initio methods are out

of question, being computationally too demanding. Force fields for silicon are not accurate enough for such covalently bonded systems. The wide range of systems, in which the sheer number of atoms is such that ab initio methods are impractical, but in which the level of accuracy required is such that empirical methods are insufficient, the tight-binding scheme is one of the best options. It has been shown that appropriately parametrized TB schemes are capable of accurately reproducing results obtained by first-principles calculations, at only a fraction of the cost [82]. In summary, TB methods lie between ab initio methods and force fields in terms of accuracy and efficiency.

Many attempts have been made to construct TB schemes for semiconductors (see review by Wang and Ho in Ref. [83]), in particular for silicon. Among them the Lenosky Si TB model has proved to be quite efficient and sufficiently accurate in many respects. Since our goal was to find out possible silicon tip-apex structures, the use of a reasonably accurate method capable of predicting genuine structures, which are verifiable a posteriori by ab initio methods, was crucial. Fortunately this was satisfied by the Lenosky Si TB at least in some tests on medium size silicon clusters which were first relaxed by TB and thereafter by density functional theory. In the original paper [77], this model has been extensively tested for small Si clusters, liquid, amorphous and bulk silicon, different crystal phases, defects in bulk silicon (vacancy and interstitial) as well as dimers on the Si(100) surface. It has proven successful almost in all of these tests. In addition, this model has been recently used by Hellmann and coworkers [79, 80, 81] to investigate medium-size clusters ($Si_n, n = 7, \dots, 19$). Using minima hopping they found new global minima for $Si_n, n = 13, 16, 19$ as well as new low-lying isomers for $Si_{13}, Si_{16}, Si_{17}, Si_{18}$. These new results were verified by one of the most accurate methods available, namely Quantum Monte Carlo. All of the impressive results mentioned above show that the Lenosky TB scheme for silicon reproduces reasonably well energy differences between structures and does an amazingly good job in the prediction of low-energy structures. These two characteristics are crucial for a model to be used for predicting silicon tip-apex structures.

In TB schemes each atom is associated with a finite set of orbitals or atomic basis states, each of which can be occupied by two electrons. A minimal (s, p) basis consisting of one s orbital and a set of three rotationally related p orbitals for each atom, have been shown to be reasonably accurate for silicon systems. The total energy E_{tot} is expressed as two terms

$$E_{tot}(\{\mathbf{r}_i\}) = E_{BS}(\{\mathbf{r}_i\}) + E_{rep}(\{\mathbf{r}_i\}) \quad (3.1)$$

$$E_{BS} = \sum_i^{occup} 2 \langle \psi_i | H_{TB} | \psi_i \rangle \quad (3.2)$$

$$E_{rep} = \sum_{i>j} \phi(|\mathbf{r}_i - \mathbf{r}_j|), \quad (3.3)$$

where the first term is the electronic energy obtained by summing the lowest eigenvalues of the TB Hamiltonian, H_{TB} , and the second term represents the repulsion of atomic

core electrons and nuclei. Two electrons are assigned to each eigenstate to account for spin. The off-diagonal elements of H_{TB} are described by rotationally invariant two-center matrix elements, $V_{ss\sigma}$, $V_{sp\sigma}$, $V_{pp\sigma}$ and $V_{pp\pi}$ between the set of sp^3 hybrid orbitals (assumed orthonormal [78]). Due to the inclusion of H atoms in our systems we needed to extend the original Lenosky TB scheme. To this aim we constructed a database consisting of the ab initio forces and energies of several Si-H clusters, bulk silicon, a H_2 molecule and a silane dimer. The Si-H cluster database consists of 40 Si-H clusters having 10,11 or 14 Si atoms and 1 to 16 H atoms. The reference energies and forces used for the fitting were obtained from plane wave density functional calculations using the local density approximation (LDA) [74] and the Perdew, Burke and Ernzerhof (PBE) [75] functional.

3.2 Search Algorithms for Low-Energy Structures

A system consisting of N atoms has $3N$ degrees of freedom, i.e. $3N$ independent coordinates $(x_1, y_1, z_1, \dots, x_N, y_N, z_N)$. Stable positions in this continuous $3N$ dimensional configuration space are minima of the potential energy surface (PES). In fact structural insight can be derived from the lowest energy configurations in a system. The true PES, which in principle can be obtained by solving the time-independent Schrödinger equation for the many-body electronic wavefunction (eigenstates of the Hamiltonian), is practically inaccessible to mankind at present. However, a large number of approximations, from classical approaches to quantum ones, have been introduced during the past century. As can be anticipated the more accurate approaches are technically more sophisticated and computationally more expensive.

Starting at a point in configurational space in order to find a minimum of PES, one uses minimization techniques such as steepest descent, conjugate gradient, etc. or sometimes combinations of them. A Multidimensional PES has an enormous number of local minima and the low-lying energy configurations are the stable ones. In particular the lowest energy structure called global minimum corresponds to the most stable structure. Finding the global minimum is thus of great importance in physics, chemistry, and biology. There is no rigorous mathematical approach to find the global minimum or even to verify whether a given minimum is the global minimum or not. The only remedy at hand to this problem is to consider the lowest energy minimum among many previously found local minima as the global minimum. The fundamental difficulty associated with global optimizations is the exponential increase of the number of local minima with respect to the number of atoms in the system. Due to this intrinsic problem finding the global minimum for medium-sized systems is already expensive and for larger systems might even be impossible with currently available computers.

A basin is the set of all points in continuous configurational space that will relax to a certain minimum using simple small-step downhill relaxation. If one can arrive from any

point in a super-basin at the lowest minimum of this super-basin without crossing barriers that are very high compared to the average difference in energy between local minima, it is called a funnel [139]. Another difficulty in global optimizations arises in systems having several funnels, for the reason that the majority of the methods are deficient and in some cases incapable of finding the global minimum if the starting point is not in the funnel containing the global minimum. There are plenty of the global optimization methods. In this dissertation we only mention briefly the most successful ones and then discuss the method we have used, called minima hopping method (MHM), its advantages especially those relevant to our requirements.

3.2.1 Overview on global optimization methods

Simulated Annealing In real life, annealing is the process in which the temperature of a molten substance is slowly reduced until the material crystallizes to give a large single crystal. It is a technique that is widely used in many areas of manufacturing, such as the production of silicon crystals for computer chips. Simulated annealing [76] is a computational method that mimics this process in order to find the global minimum. Initially at a given high temperature the system is allowed to reach approximately thermal equilibrium using a molecular dynamics or Monte Carlo simulation. At high temperatures, the system is able to sample high energy regions of configurational space and to pass over high energy barriers. As the temperature falls, lower energy configurations become more probable in accordance with the Boltzmann distribution. Eventually at very low temperature, the system is expected to occupy the lowest-energy configuration. Moreover, this is true only for systems with uncomplicated energy landscapes.

Basin Hopping Method Basin Hopping (BHM) [84, 85] is a method in which the PES is mapped into a collection of interpenetrating staircases. This transformation associates any point in the configurational space with the local minimum obtained by a geometry minimization started at that point, $\tilde{E}(X) = \min\{E(X)\}$ where X represents the $3N$ -dimensional vector of the nuclear coordinates and \min signifies that an energy minimization is performed starting from X . In this way transition state regions are effectively removed from the problem. Moreover, it does not change the global minimum, nor the relative energies of any local minima. The transformed energy landscape $\tilde{E}(X)$ is then explored using a canonical Monte Carlo simulation at a constant temperature. At each step, all coordinates are displaced by a random number in the range $[-1, 1]$ times the step size, which is dynamically adjusted to give an acceptance ratio of 0.5. Basin hopping can also be used within a simulated annealing scheme if the only free parameter of the basin hopping method, namely the temperature T is lowered gradually during the simulation.

Genetic algorithms Genetic algorithms [86, 87, 88, 89, 90] are a particular class of evolutionary algorithms (also known as evolutionary computation) and are among

the most successful global optimization methods. They were originally inspired by Darwin's theory of evolution, more precisely they mimic the evolution processes in biology with inheritance and mutation from parents built into each new generation as the key elements. The first step in the implementation of any genetic algorithm is to generate an initial population of configurations, which is called the initial gene pool. In the next step one selects the gene candidates to create the next generation. The way to mix the selected genes of the two parents is called crossover, which reflects how the genetic attributes are passed on. Another effective way of exploring the PES in genetic algorithms is through the mutation process. In each of the three main operations (selection, crossover, mutation) in each generation, one makes sure that the elite configurations with the lowest energies always survive.

3.2.2 Minima hopping method

Like genetic algorithms, MHM is a non-thermodynamic-based global optimization method. It is based on a feedback mechanism introduced by the history list of all the previously visited minima. MHM has two parts: The first part, starting from a given minimum, makes attempts to jump into the basin of another local minimum. And then follows a geometry minimization to find the local minimum of that basin; The second part concerns accepting or rejecting the found minimum. It is accepted if the energy of the found minimum E_{new} is less than $E_{cur} + E_{diff}$ (E_{cur} is the energy of the current minimum and $E_{diff} > 0$), otherwise the found minimum is rejected. In this way the second part introduces a preference for steps that go down in energy. This drives the simulation to explore mainly the low-energy region of configurational space as well as temporarily the high-energy region if needed. The parameter E_{diff} is adjusted dynamically during the simulation in such a way that half of the moves are accepted and half of them are rejected.

The jumps in the first part of a MHM cycle can be performed by using random displacement or eigenvector following methods, however we have utilized Molecular Dynamics (MD) because, as shown in Ref. [91], MD is far better than the other two options mentioned above. In all cycles of MHM, MD is started at the current local minimum with atoms given a Boltzmann velocity distribution with random velocity directions such that the total kinetic energy is equal to E_{kin} . The MD simulation is stopped as soon as the potential energy has crossed $mdmin$ maxima and reached the $mdmin$ -th minimum along the MD trajectory. If E_{kin} is small, one usually falls back into the current minimum and E_{kin} , in the second part of the MHM, is multiplied by β_1 ($\beta_1 > 1$). If β_1 is sufficiently big, one will most likely be ejected from the current basin and end up in a different minimum. Totally five parameters $\{\beta_1, \beta_2, \beta_3\}$ and $\{\alpha_1, \alpha_2\}$ are used to adjust E_{kin} and E_{diff} respectively. These adjustments are done dynamically during the simulation in the second part of MHM with regard to the history list of all previously visited minima. As mentioned before, the role of β_1 is to increase E_{kin} whenever MD has failed to jump into another minimum. E_{kin} is increased by the factor β_2 ($\beta_2 > 1$) whenever MD succeeds to jump

into another minimum basin but a previously visited one. Finally when a new (unvisited) minimum is found, E_{kin} is multiplied by β_3 ($\beta_3 < 1$). Decreasing E_{kin} , whenever a new (unvisited) minimum is found, helps the simulation jump into another basin by crossing low barriers. This is a very important feature of MHM for the reason that in this way the Bell-Evans-Polanyi (BEP) principle [92] is satisfied in an average sense. The BEP principle states that low energy molecular dynamics trajectories are more likely to cross into the basin of attraction of a low energy local minimum than high energy trajectories [92]. An instructive flowchart of MHM is presented in Ref. [91].

3.2.3 Why minima hopping method?

Simulated annealing, in general, is inefficient; hence it is not suitable for large systems using a TB scheme. Two points are concerned BHM. One is the fact that BHM is based on thermodynamic principles which nearly guarantee to find the global minimum but can not guarantee how fast it does. We use a TB scheme for the energy and the force evaluations and our systems are rather large so that efficiency is an ultimate concern in our simulations. The other is that in the BHM the hopping process is performed using random displacement and, as mentioned in Ref. [91], it is not as efficient as MD due to the fact that the BEP principle is ignored. In principle MD could be used instead but we are not aware of any report using MD in the BHM.

Genetic algorithms could possibly satisfy the required efficiency, but temperature does not play any role in these algorithms. Let's assume we crash a silicon tip into the sample (say a silicon surface). The tip-apex structure at the instant right after the crashing is most probably initially sharp; thereafter the system relaxes into a low energy basin of the PES at a finite temperature namely the temperature of the surrounding material within the experiment time scale. Using a genetic algorithm we cannot mimic this process i.e., limiting oneself to start with a single configuration and seek accessible low energy configurations of the PES. Genetic algorithms start with many configurations which may locate in completely different part of the PES. Moreover, genetic algorithms imply violent movements, e.g. in the mutation part. However, one can assume that by eliminating mutations as well as limiting the initial gene pool, that it might be possible to develop a genetic algorithm suitable for our purpose. But the efficiency of such a genetic algorithm would be strongly limited by such restrictions. In fact, we wish to find the structures not necessarily the global minimum but the lowest energy configurations accessible on experimental time scales, especially the time interval used to probe the sample at any given position.

In the MHM we start with a particular configuration, the temperature is dynamically adjusted during the simulation and we can readily limit it to the experimental temperature used for tip preparation. MHM has been extensively used for silicon clusters and Lennard-Jones clusters and it has been shown that MHM is quite efficient. Taking into account

all these facts, the MHM is *presumably* optimal for our goal.

3.3 Silicon Tip Structures

There have been many attempts to simulate SPM experiments in which a silicon tip acts as the probe [65, 66, 67, 68, 69, 93, 94, 96, 97]. In all these simulations, small and medium size constrained silicon clusters have been used as model tips. The structure of the silicon model tips was derived in part intuitively from information on the ground state of unconstrained small silicon clusters or from knowledge about reconstructed silicon surfaces [95]. Even though using such informed guesses to construct silicon model tips is not unreasonable, real silicon tip-apexes do not necessarily exhibit the characteristic features of small unconstrained silicon clusters or of silicon surfaces. This has been shown by some of our results. Indeed the main limitation of small model tips stems from the reduced size of the nanoasperities imposed by the large computational cost of ab initio methods. These small systems can only pretend to describe the atomic structure of the 4-6 outermost apex atoms while the other atoms are strongly affected by the imposed boundary conditions. Therefore these systems do not provide reliable information about further atomic layers.

The energy landscape of a system consisting of N atoms strongly depends on N ; in an extreme example it is worth mentioning that bulk gallium melts at room temperature (302.9 K) while some small gallium clusters remain solid up to 800K. Due to these reasons and those discussed in Ref. [71], we consider that silicon model tips consisting of tens to hundreds of Si atoms would be more realistic and likely mimic the characteristic features of real silicon tip-apexes. Using the minima hopping method, we have performed simulations on H-terminated Si clusters as model tips as well as a Si cluster on a Si surface. Our H-terminated Si clusters consist of $Si_{70}H_{50}$, $Si_{71}H_{50}$, $Si_{72}H_{50}$ and $Si_{238}H_{118}$. We consider the first three model tips medium and the fourth one large. In all of these medium-size tips, 47 Si atoms in the base of the model tips as well as the saturating H atoms are fixed in bulk positions. In the apex of these model tips, 23, 24 and 25 Si atoms respectively in systems $Si_{70}H_{50}$, $Si_{71}H_{50}$ and $Si_{72}H_{50}$ are allowed to move in the different parts of the MHM.

The limited size of the four different model tips as well as the limitation imposed by the frozen passivating H atoms could affect our results. To test this idea we simulated a Si cluster on a Si surface as well. The surface was represented by a slab with periodic boundary condition in the lateral directions. The lateral size of the surface is chosen to be large enough to eliminate any interaction among the cluster and its images and also to have enough uncovered atoms so that the cluster can diffuse on the surface.

Our goal was mainly to search for low-energy configurations. In some AFM experiments such as in Ref. [99, 98] the AFM tip is annealed up to 1200 K to remove oxide layer

covering the tip. It is very likely that after annealing the apex of the tip relaxes to the lowest-energy configuration or to one of the configurations close in energy. We therefore limited the temperature in the MHM to 1200 K. We found 5000, 7004 and 6441 local minima for $Si_{70}H_{50}$, $Si_{71}H_{50}$, $Si_{72}H_{50}$ respectively. Only the atomic positions of the low-energy configurations were retained. Since our first model tip, $Si_{70}H_{50}$, had 23 unfrozen Si atoms, this limitation could have influenced the outcome of the simulation. One way to investigate the effect of this limitation is to consider models tips which only differ by only one or two unfrozen atoms. The systems $Si_{71}H_{50}$, $Si_{72}H_{50}$ have therefore also been investigated.

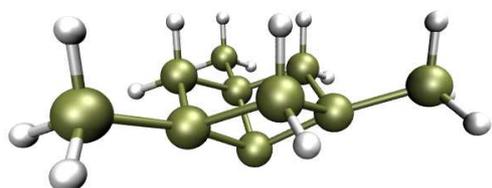
3.3.1 Small silicon model tips

The small model tips shown in Fig. 3.1 were derived from well-known stable semiconductor surface terminations. The H3 model tip, shown in the Fig. 3.1(a), mimics a rest-atom of the reconstructed Si(111) and Ge(111) surfaces. The T4 model tip, shown in the Fig. 3.1(b), is related to an adatom configuration. The dimer model tip [100] has some similarities with dimers of the reconstructed Si(100) surface. Small tips with the H3, T4 and dimer terminations have been successfully used previously to simulate the interaction between the tip and semiconductor surface [66, 67, 64, 65, 69]. In these studies, the tips were made of different atoms: pure Si tips, pure Ge tips and in some cases Si tips were contaminated with a Sn atom. But in all these cases, the H3 and T4 tips showed a qualitatively different behavior from the dimer tip, e.g. the calculated short-range forces upon the approach and retraction of the dimer tip and the T4 tip over an adatom of the reconstructed Ge(111) c(2x8) surface. In the case of the T4 tip both force curves are very similar while a clear hysteresis between the two force curves appears for the dimer tip (for details see Ref. [67]).

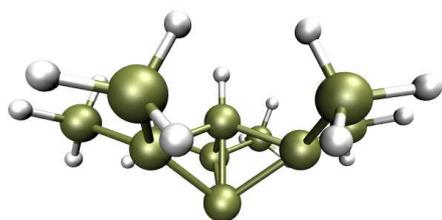
H3 and T4 tips are characterized by a single outermost atom which has a dangling bond. The dimer tip is characterized by the presence of two atoms with dangling bonds. The main difference with the one-dangling bond tips is that the two dangling bonds interact between themselves and with the surroundings. This interaction modifies the charge state of the dangling bonds inducing a charge transfer that minimizes the energy. This process is similar to that which stabilizes the tilted dimers of the Si (100) surface reconstruction. The foremost atom in the model tip H3 is three-fold coordinated and in the T4 model tip is four-fold coordinated. In H3 model tip, the four outermost Si atoms are allowed to move and the rest of Si atoms, which are passivated by H atoms, as well as H atoms are kept fixed during our simulations. In T4 model tip, the four outermost Si atoms as well as the Si atom (passivated by one H atom) right above the apex atom are allowed to move and the rest of Si atoms, which are passivated by H atoms, as well as H atoms are kept fixed during our simulations. In dimer model tip, the upper 21 Si atoms which are nearly located in bulk positions as well as H atoms are kept fixed and the rest of eight Si atoms located at the apex are allowed to move during our simulations.

The theoretical force-distance curves for these small tips capture basic features of the experimental short range forces. These results also show that the interaction between the tip and the surface depends strongly on the structure of the tip termination, e.g. a change in the neighborhood of the outermost tip atom produces a variation of the maximum attractive force value larger than 10%. Notice that the observed variation of the minimum short range forces is smaller than that observed in the experiment shown in Ref. [65].

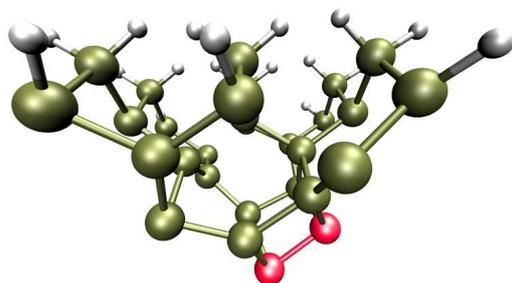
These small model tips have been successful to explain to some properties of the short range interaction between the tip and exposed surface atoms. However, each one is best suited for a certain purpose, so that one should not expect to obtain reasonable results for different properties using only a single model tip. For example, the T4 model tip cannot resolve the rest-atoms on the reconstructed Si(111) 7×7 surface because when the tip is over a rest atom, the atoms in the second layer of the tip start to interact with the adatoms surrounding the rest-atoms. Furthermore, for such small model tips, atoms tightly bounded to the tip base atoms lead to a large stiffness of the tip which prevents processes such as sharpening, which could help resolving the rest-atoms. Furthermore, the restriction arising from small tip size prevents one to reveal important processes in atomic-scale friction or dissipation. In chapter four, using our medium-size Si model tips obtained by the MHM, we reveal new dissipation mechanisms in the dynamic force microscopy arising from the tip alone.



(a) The H3 model tip.



(b) The T4 model tip.



(c) The dimer model tip.

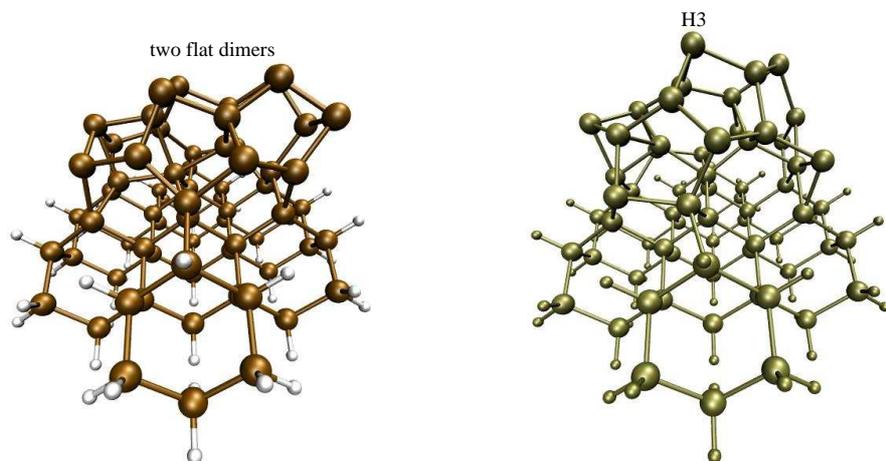
Figure 3.1: The configurations of H3, T4 and dimer model tips.

3.3.2 Medium-size partially H-passivated Si cluster $Si_{70}H_{50}$

To search for possible tip-apex structures of medium-size Si model tips, we started with a tip consisting of 70 Si atoms and 50 H atoms. The model tip has an approximately pyramidal shape and 23 Si atoms in the tip-apex were allowed to move in the different parts of the MHM while the rest of the Si atoms together with the H atoms were fixed. The temperature in the molecular dynamics part of the MHM was limited to 1200 K. After finding 5000 minima, and keeping the full geometry of the 400 lowest energy structures, the program was stopped after two weeks because no new low energy structure was found. In accordance to the thermodynamic point of view discussed before, we show the three lowest energy structures of the model tip $Si_{70}H_{50}$ in Figs. 3.2(a), 3.4(a), and 3.4(b). The second and the third lowest structures were the only ones whose energies are less than 0.1 eV with respect to the energy of the ground state. Their energies are given in Table 3.1. The ground state configuration of the $Si_{70}H_{50}$ is blunt, where the second and the third lowest ones are less blunt and quite asymmetric.

Table 3.1: The Tight-Binding energies in eV for the lowest 3 configurations of $Si_{70}H_{50}$. The lowest energy is set to 0.

lowest	2nd	3rd
0.0	0.0587	0.0700



(a) The lowest energy structure of $Si_{70}H_{50}$. (b) The lowest energy structure of $Si_{71}H_{50}$.

Figure 3.2: The lowest energy structures of $Si_{70}H_{50}$ and $Si_{71}H_{50}$

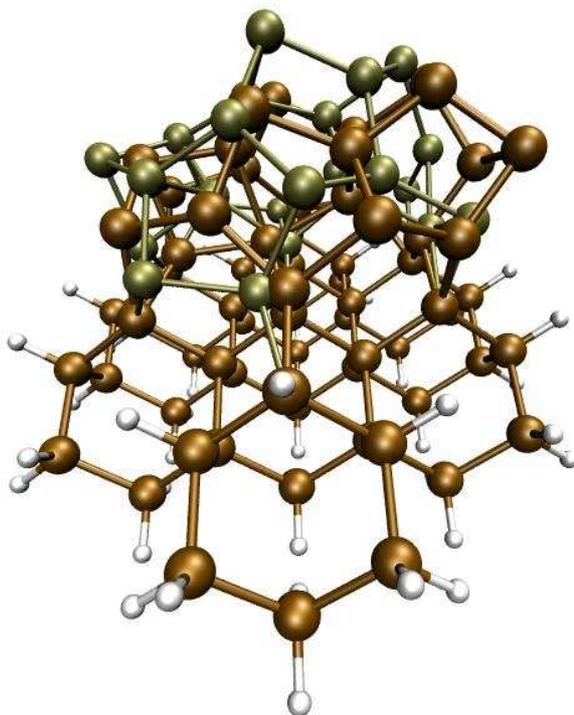
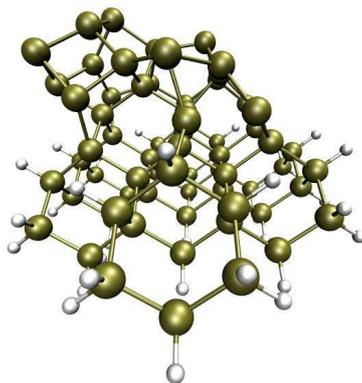
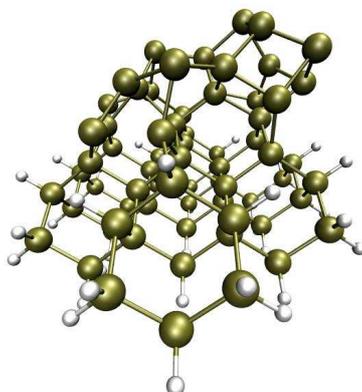


Figure 3.3: Superimposition of the lowest energy structures of $Si_{70}H_{50}$ and $Si_{71}H_{50}$



(a) The 2nd lowest energy structure of $Si_{70}H_{50}$



(b) The 3rd lowest energy structure of $Si_{70}H_{50}$

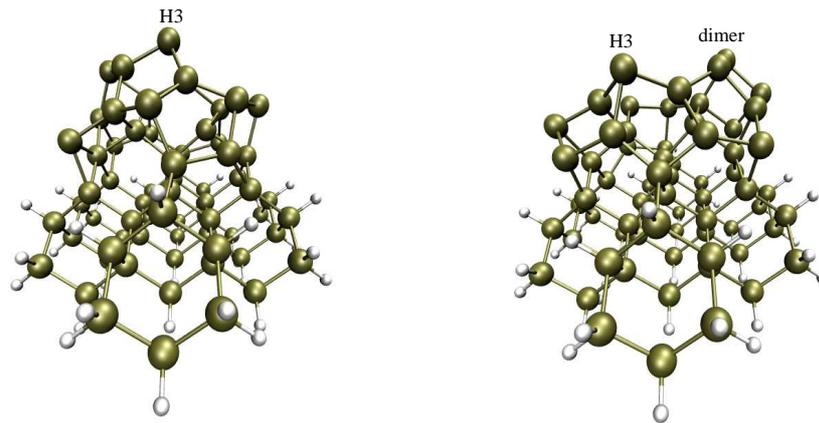
Figure 3.4: The 2nd and the 3rd lowest energy structures of $Si_{70}H_{50}$. They are nearly mirror symmetric.

3.3.3 Medium-size partially H-passivated Si clusters $Si_{71}H_{50}$

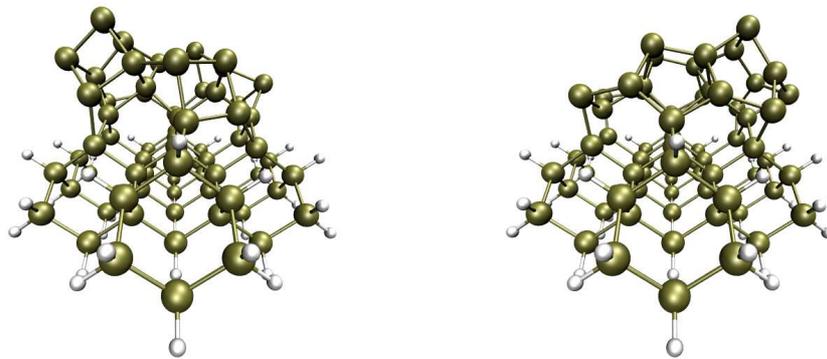
Similar to $Si_{70}H_{50}$, we initiated a MHM run on the model tip $Si_{71}H_{50}$ starting with a configuration which had pyramidal shape. 24 Si atoms in the tip-apex were allowed to move in the different part of the MHM and the rest were fixed in bulk positions. In fact one extra atom was added at the apex of the $Si_{70}H_{50}$ model tip. As before the maximum value for the temperature of the molecular dynamics part of the MHM was set to 1200 K. We stopped the simulation with the same condition as that for the $Si_{70}H_{50}$ model tip. 7004 minima were found. Interestingly, there are nine configurations which energies lie between 0.1 eV with respect to the lowest one. These configurations are shown in the Figs. 3.2(b), 3.5 and 3.6. The relevant energies are presented in the Table 3.2. Unlike $Si_{70}H_{50}$, the ground state of the model tip $Si_{71}H_{50}$ is sharp. Moreover, most of the other eight configurations are also sharp and only those shown in Figs. 3.5(b) and 3.6(b) are nearly blunt. Thus most of the configurations among the nine ones are likely to form multicontacts when interacting with the sample surface, although there are enough Si atoms free to lead to a multicontact as suggested by the results for the $Si_{70}H_{50}$ model tip.

Table 3.2: The Tight-Binding energies in eV for the lowest 9 configurations of $Si_{71}H_{50}$. The lowest energy was chosen as reference energy and set to 0.

lowest	2nd	3rd	4th	5th	6th	7th	8th	9th
0.0	0.0052	0.0435	0.0435	0.0623	0.0657	0.0886	0.0887	0.0894

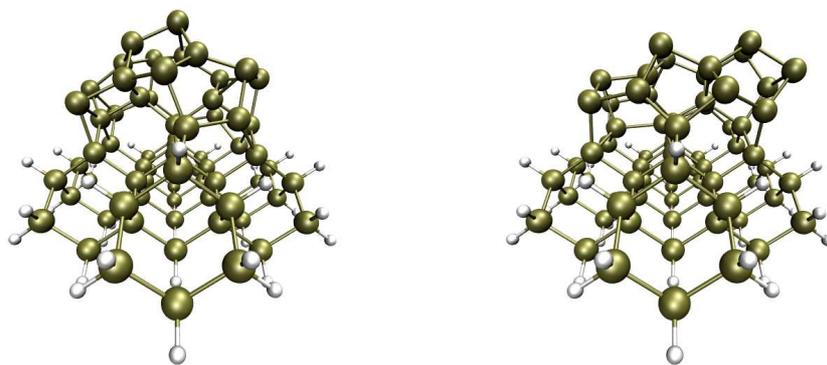


(a) The 2nd lowest energy structure of $Si_{71}H_{50}$ (b) The 3rd lowest energy structure of $Si_{71}H_{50}$

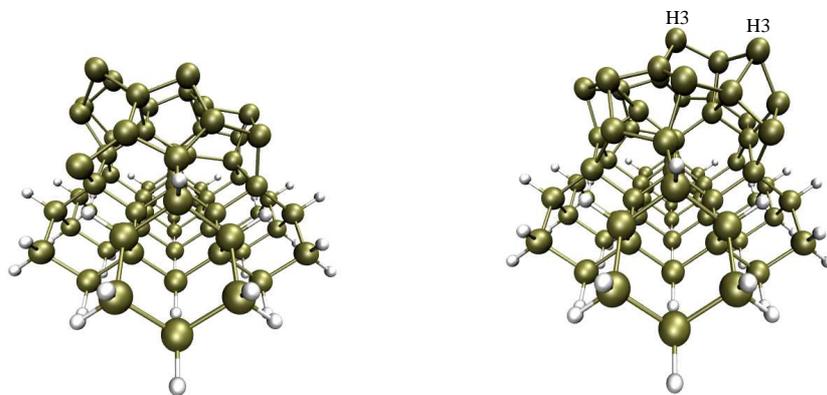


(c) The 4th lowest energy structure of $Si_{71}H_{50}$ (d) The 5th lowest energy structure of $Si_{71}H_{50}$

Figure 3.5: The 2nd-5th lowest energy structures of $Si_{71}H_{50}$. The lowest one of this model tip is in Fig. 3.2(b)



(a) The 6th lowest energy structure of $Si_{71}H_{50}$ (b) The 7th lowest energy structure of $Si_{71}H_{50}$



(c) The 8th lowest energy structure of $Si_{71}H_{50}$ (d) The 9th lowest energy structure of $Si_{71}H_{50}$

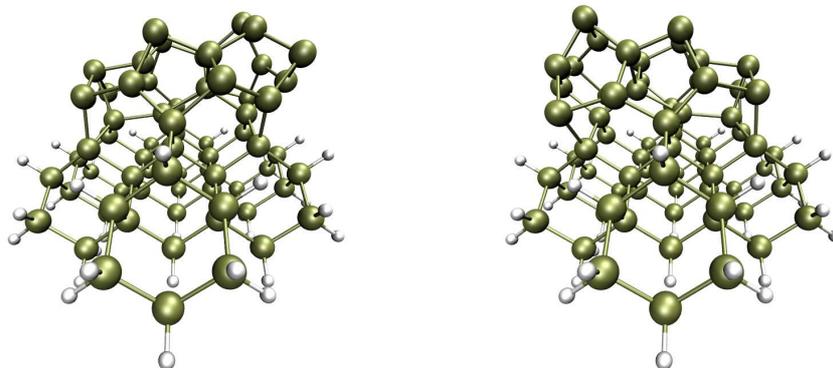
Figure 3.6: The 6th-9th lowest energy structures of $Si_{71}H_{50}$.

3.3.4 Medium-size partially H-passivated Si clusters $Si_{72}H_{50}$

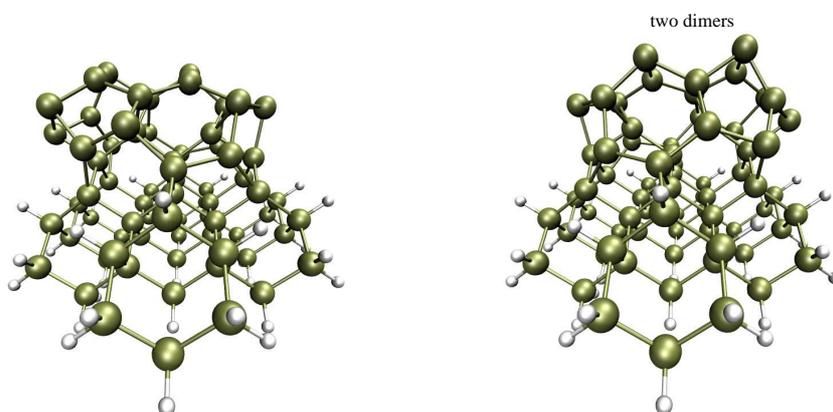
This model tip was treated in a similar approach as $Si_{70}H_{50}$ and $Si_{71}H_{50}$. 6441 minima were found while only the six lowest energy structures have energies within 0.1 eV. These structures are shown in Figs. 3.7a-f and the corresponding energies are given in Table 3.3. These configurations, unlike those of $Si_{71}H_{50}$ and similar to those of $Si_{70}H_{50}$, are nearly blunt except the 4th, 5th, and 6th which have higher energies. In all of these six configurations most of 24 unfrozen Si atoms have three-fold coordination.

Table 3.3: The Tight-Binding energies in eV for the lowest 6 configurations of $Si_{72}H_{50}$. The lowest energy was chosen as reference energy and set to 0.

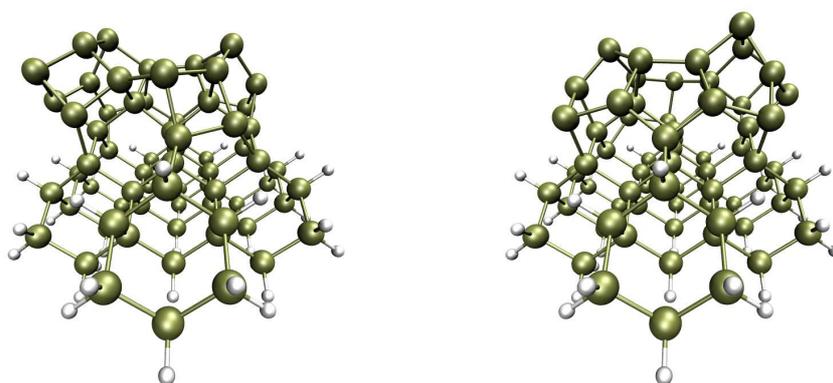
lowest	2nd	3rd	4th	5th	6th
0	0.0001	0.0611	0.0611	0.0831	0.0832



(a) The lowest energy structure of $Si_{72}H_{50}$. (b) The 2nd lowest energy structure of $Si_{72}H_{50}$



(c) The 3rd lowest energy structure of $Si_{72}H_{50}$ (d) The 4th lowest energy structure of $Si_{72}H_{50}$



(e) The 5th lowest energy structure of $Si_{72}H_{50}$ (f) The 6th lowest energy structure of $Si_{72}H_{50}$

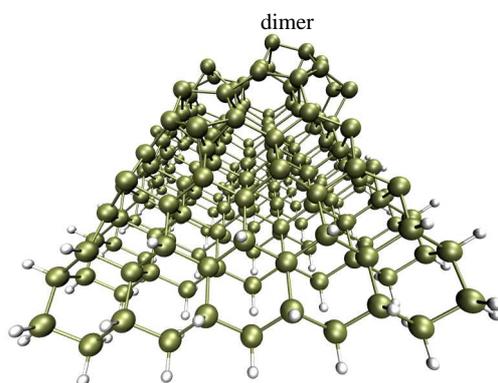
Figure 3.7: The 1st-6th lowest energy structures of $Si_{72}H_{50}$.

3.3.5 Large partially H-passivated Si clusters ($Si_{238}H_{118}$)

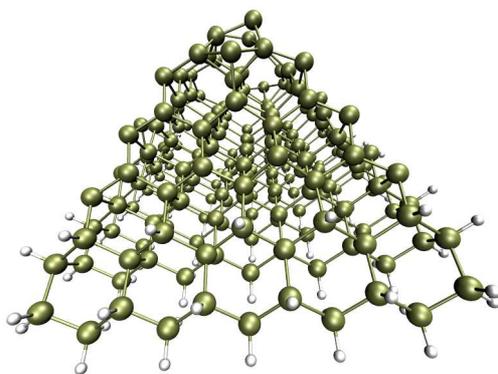
In the previous sections we demonstrated structural changes due to the number of atoms in three model tips. Those medium model tips are likely large enough to be used in an AFM simulation. In fact this hypothesis has been justified by the results, presented in the next chapter, in which novel mechanisms in atomic-scale dissipation have been revealed using the low-energy structures of the $Si_{72}H_{50}$ model tip. We also started a global optimization of a constrained large Si-H cluster using MHM. The system consists of 238 Si atoms and 118 H atoms totally in 9 layers. 95 Si atoms in 5 layers of the tip-apex are allowed to move in the different parts of the MHM while the remaining 143 Si atoms together with all the H atoms are fixed in bulk positions. The frozen Si atoms are in 4 base layers and all of them are passivated by H atoms either from bottom or sides. We stopped the simulation after finding 14023 minima due to lack of progress in the simulation for a long time. Similar to the medium-size model tips, we found several low-lying energy structures within 0.1 eV. There are eight such configurations depicted in Figs. 3.8, 3.9, and 3.10. The corresponding energies of the eight structures respect to the lowest one are listed in Table 3.4. Most of them are sharp and the apex configuration is similar to the small dimer model tip in Fig. 3.1(c). The Si atoms of the intermediate layers of the ground state are almost in bulk position. The 4th lowest and 8th lowest configurations have two counterlike dimers at the apex while 4th lowest and 7th lowest configurations have two parallel dimers at the apex. The fifth lowest energy structure of $Si_{238}H_{118}$ can be considered a multicontact tip, one contact is similar to small H3 model tip and the other is similar to small dimer model tip.

Table 3.4: The tight-binding energies in eV for the lowest 8 configurations of $Si_{238}H_{118}$. The lowest energy was chosen as reference energy and set to 0.

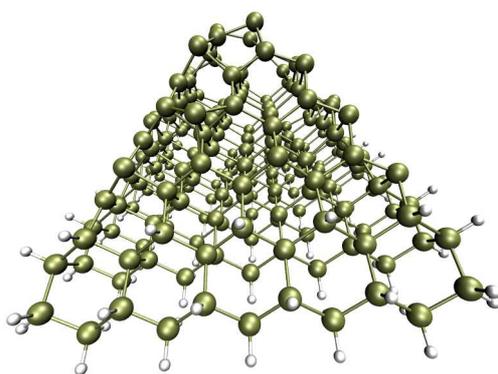
lowest	2nd	3rd	4th	5th	6th	7th	8th
0.0	0.00113	0.03332	0.07479	0.07677	0.08581	0.08694	0.09404



(a) The lowest energy structure of $Si_{238}H_{118}$.

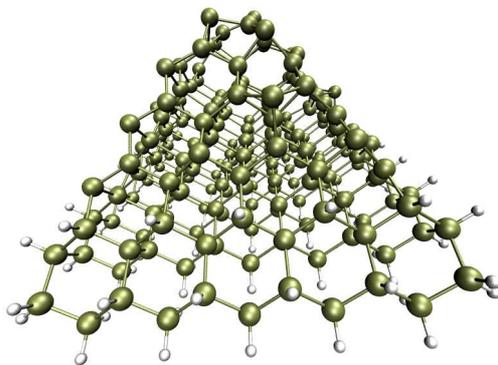


(b) The 2nd lowest energy structure of $Si_{238}H_{118}$.

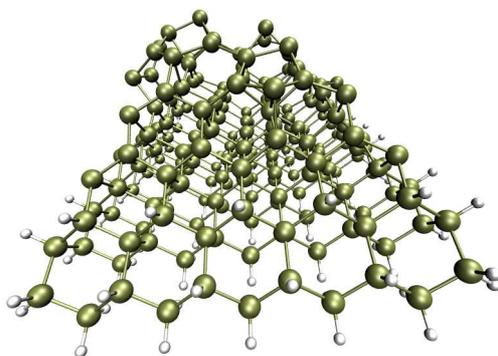


(c) The 3rd lowest energy structure of $Si_{238}H_{118}$.

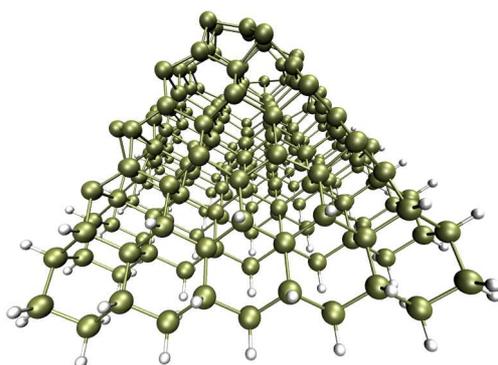
Figure 3.8: The 1st-3rd lowest energy structures of $Si_{238}H_{118}$.



(a) The 4th lowest energy structure of $Si_{238}H_{118}$

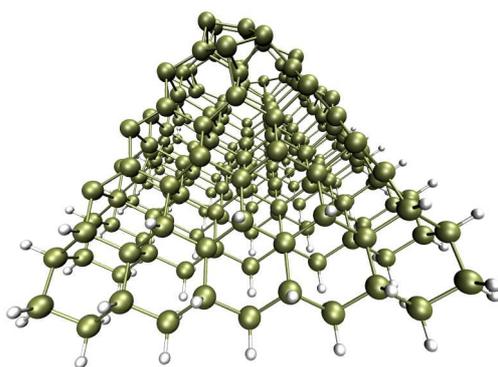


(b) The 5th lowest energy structure of $Si_{238}H_{118}$

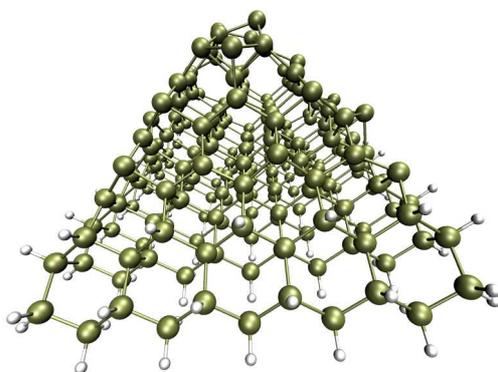


(c) The 6th lowest energy structure of $Si_{238}H_{118}$

Figure 3.9: The 4th-6th lowest energy structures of $Si_{238}H_{118}$.



(a) The 7th lowest energy structure of $Si_{238}H_{118}$



(b) The 8th lowest energy structure of $Si_{238}H_{118}$

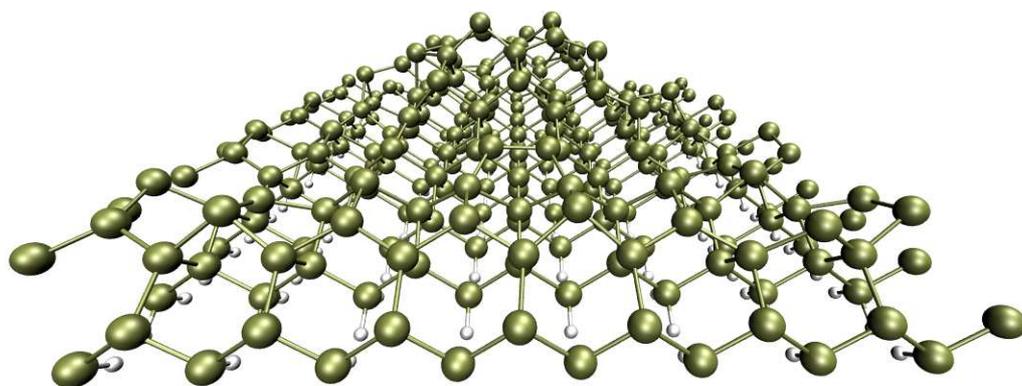
Figure 3.10: The 7th-8th lowest energy structures of $Si_{238}H_{118}$.

3.3.6 A Si cluster on a reconstructed Si(001) 2×1 surface

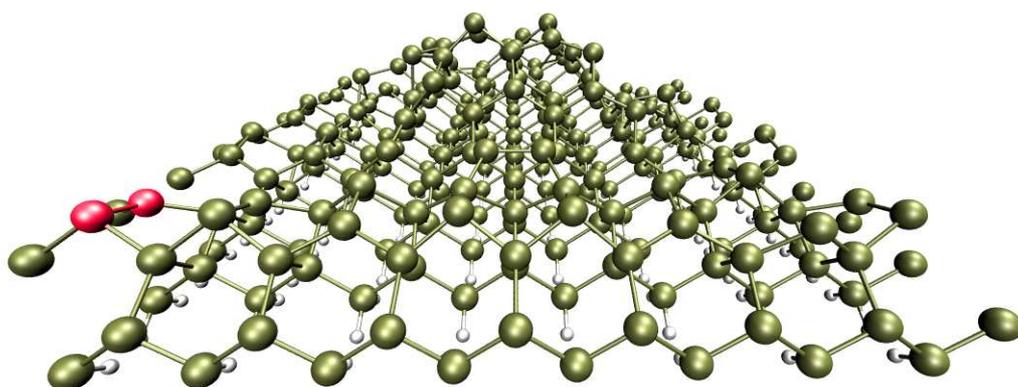
The previously discussed model tips all have fixed base layers passivated by H atoms whereas in a real tip, probably more apex atoms have the freedom to move around. To investigate this issue, we located a sharp Si cluster with pyramidal shape on a reconstructed Si(001) 2×1 surface with tilted dimers. The system consists of 306 Si atoms and 128 H atoms, 178 Si atoms including all atoms of the cluster and in the top two layers of the surface are allowed to move in the different parts of the MHM. Again several low-lying energy configurations are found. Five of such structures whose energies are less than 0.1 eV with respect to the lowest one are depicted in Figs. 3.11, 3.12, and 3.13. An interesting feature of these structures is that most have the same apex and differ only by one or two flipped dimers on the surface. The only exception is the third lowest one which has a slightly different apex, namely two parallel tilted dimers instead of two dimers tilted in opposite directions.

Table 3.5: The tight-binding energies in eV for the lowest 5 configurations of the system consisting of a Si cluster on a Si(001) surface, totally including 306 Si atoms and 128 H atoms. The lowest energy was chosen as the reference energy and set to 0.

lowest	2nd	3rd	4th	5th
0.0	0.00182096	0.0960037	0.105853	0.105964

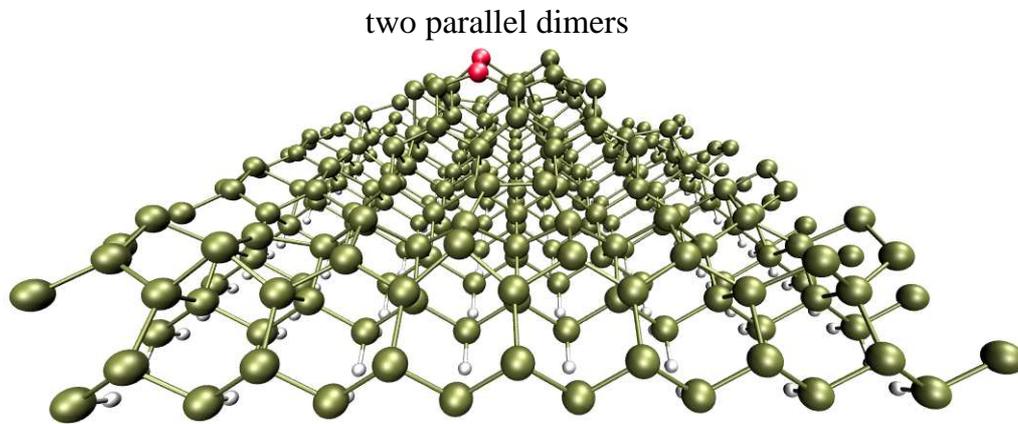


(a) The lowest energy structure of the cluster Si_{50} on Si(001).

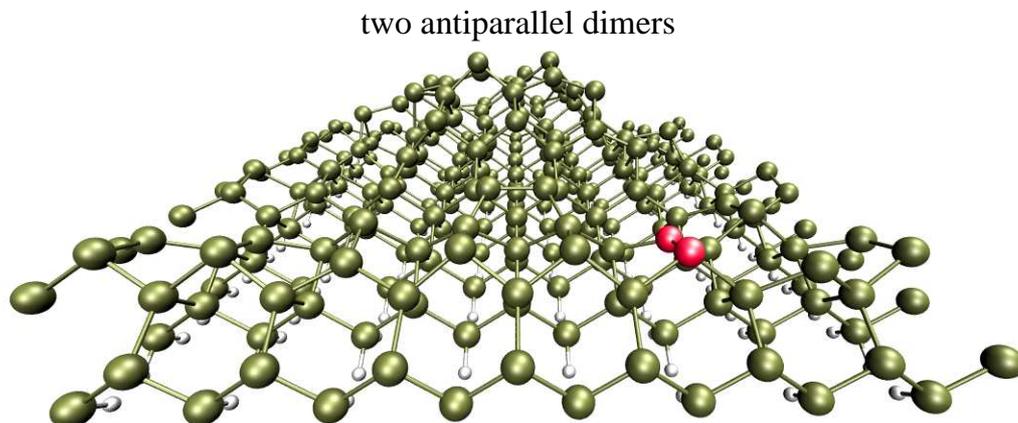


(b) The 2nd lowest energy structure of the cluster Si_{50} on Si(001).

Figure 3.11: The 1st-2nd lowest energy structures of the cluster Si_{50} on Si(001).



(a) The 3rd lowest energy structure of the cluster Si_{50} on Si(001).



(b) The 4th lowest energy structure of the cluster Si_{50} on Si(001).

Figure 3.12: The 3rd-4th lowest energy structures of the cluster Si_{50} on Si(001).

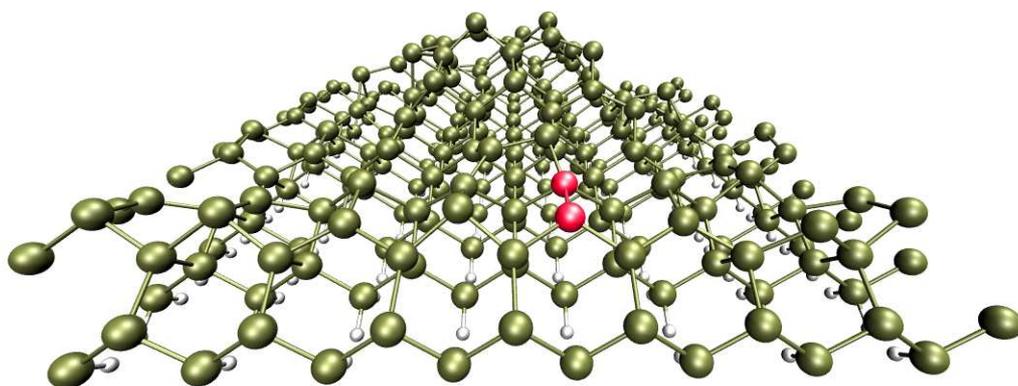


Figure 3.13: The 5th lowest energy structure of the cluster Si_{50} on Si(001).

3.3.7 The stiffness of the investigated model tips

In this section we analyze elastic properties of the model tips investigated in the previous sections. These properties provide direct insights into the mechanical response of tip induced by tip-sample interactions considered in the next chapter. The outermost under-coordinated tip-apex atom interacts most strongly and makes the largest contribution to the short range interaction between the Si tip and dangling bonds on a Si surface. Therefore, one can assess the mechanical response of a model tip by analyzing the stiffness of the model tip with respect to displacements of the outermost apex atom. To this aim, the vertical and the lateral stiffnesses (in two orthogonal directions) were calculated for all lowest-energy structures of the small, medium, large, and cluster on surface model tips. Although the stiffness of a model tip associated with all displacements of the outermost tip-apex atom is a tensor with rank two, we considered as univariable function i.e. its diagonal elements, because we are interested mainly in the strongest mechanical response to vertical and lateral forces.

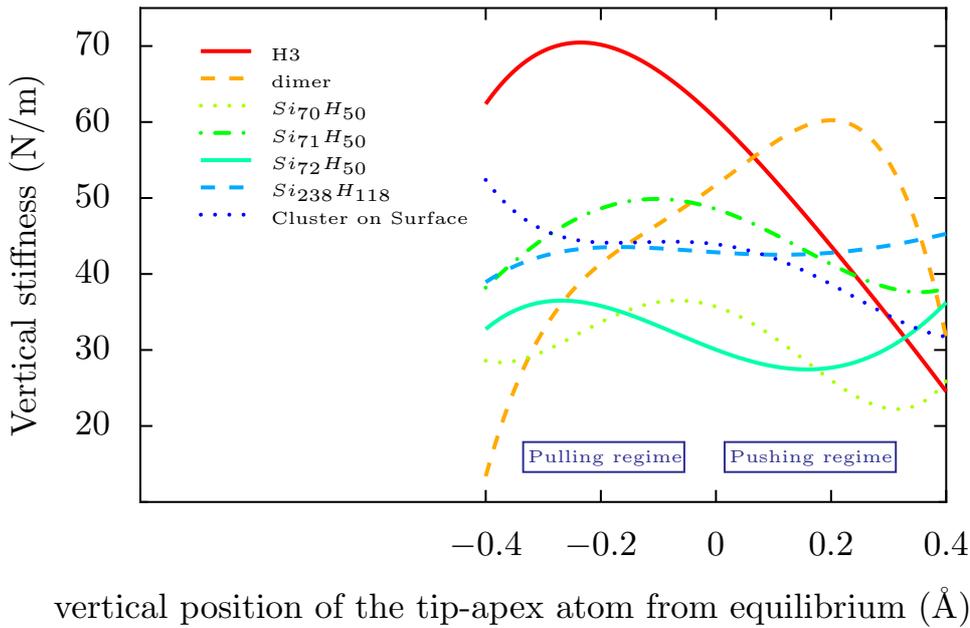


Figure 3.14: The vertical stiffness of the investigated model tips $H3$, dimer, $Si_{70}H_{50}$, $Si_{71}H_{50}$, $Si_{72}H_{50}$, $Si_{238}H_{118}$, $Si_{50}/Si(001)$.

These diagonal stiffnesses are the second derivatives of the potential energy with respect to displacements of the foremost atom in three orthogonal directions. In practice, starting from the relaxed structure, the outermost tip-apex atom is displaced in one direction, say z , an energy minimization is performed, while keeping fixed the previously frozen atoms together with the outermost tip-apex atom. In this way, the vertical stiffness is calculated and shown in Fig. 3.14. The behavior of the small model tips is much more variable for a given displacement. The $H3$ tip becomes much stiffer if the outermost tip-apex atom is

pulled and softer if the outermost tip-apex atom pushed. The dimer model tip exhibits the opposite trend. The T4 model tip which is shown in Fig. 3.16 is stiffer than all the other model tips almost by a factor of 3. As expected the medium and large model tips are softer than the small model tips and exhibit only a small variation, i.e. nearly linear elasticity. The estimated tip-apex stiffness of real Si tips is about 1 N/m and using continuum mechanics it is possible to show that this value change only little within the range $[-0.4, 0.4]$ angstrom. Despite the fact that our medium and large model tips are still much stiffer than a real Si tip, they reasonably mimic the behavior of real Si tips, i.e. these model tips exhibit approximately constant stiffnesses. In contrast to these model tips, the small model tips do not behave consistently and become very stiff or very soft. This is even more drastic for the stiffness in the lateral directions. Lateral stiffness is ill-defined except for infinitesimal displacements. In our calculations, we displace the foremost tip-apex atom in orthogonal x and y directions labelled I and II respectively. The T4 model tip is softer than all the others in direction I , which varies only slightly. But its stiffness in direction II varies drastically. H3 is similar in the sense that it is soft but stable in one lateral direction and very nonlinear in the other direction. Among the small model tips only the dimer one behaves normally but in the lateral directions. In summary, none of the small model tips are likely to adequately represent realistic tips. On the other hand, almost all of our presented model tips have similar behavior and are suitable for more realistic AFM simulations.

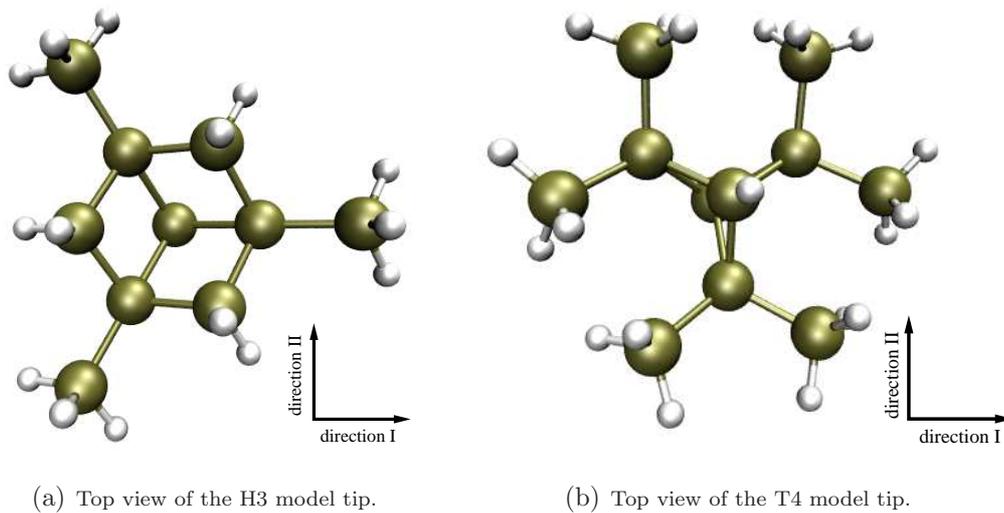


Figure 3.15: The H3 and T4 model tips are illustrated in top view and directions I and II are identified.

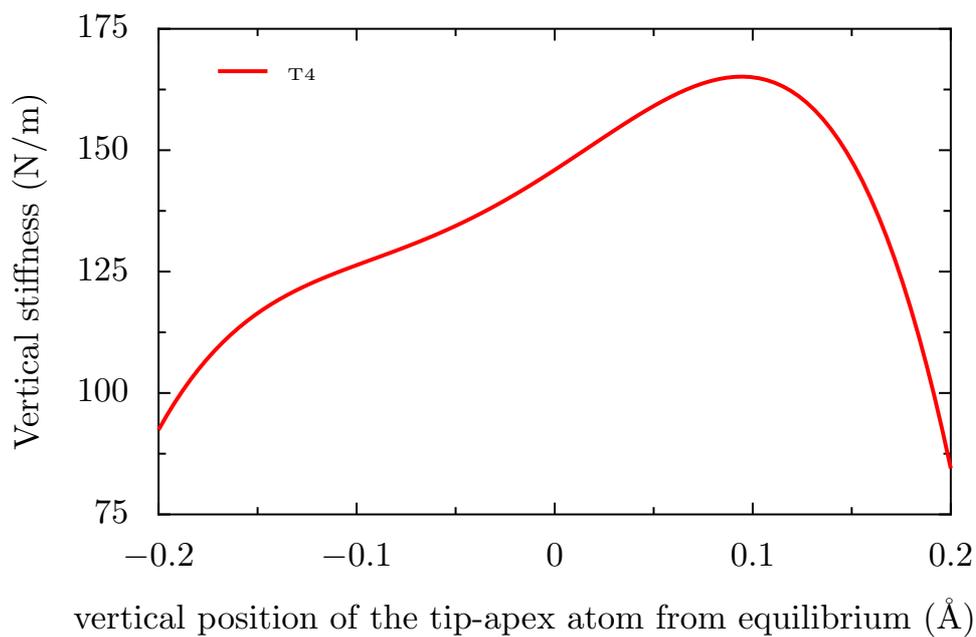


Figure 3.16: The vertical stiffness of the model tip $T4$.

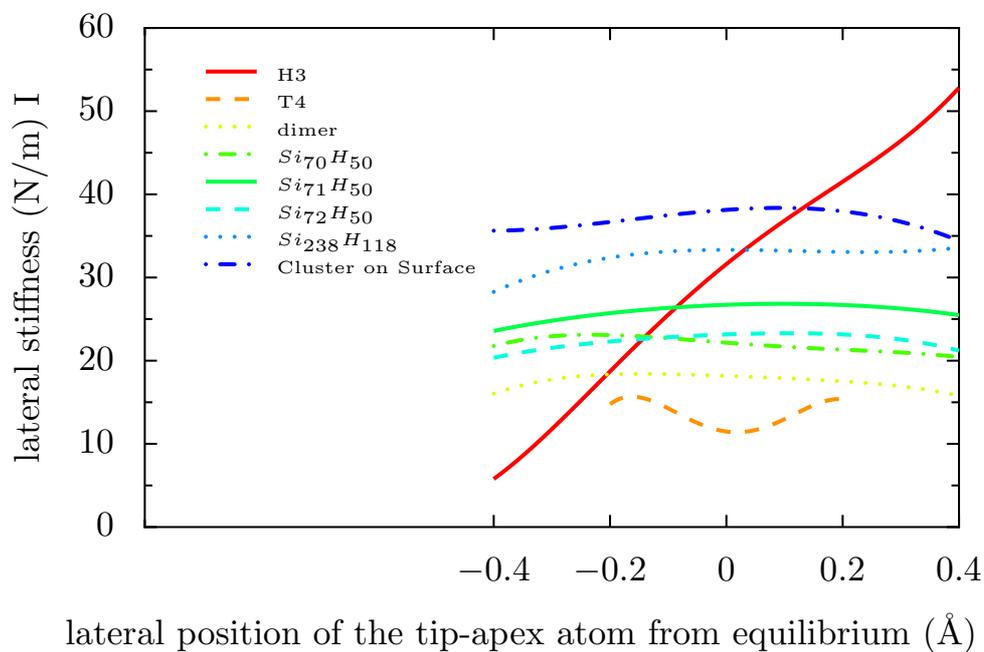


Figure 3.17: The lateral stiffness I of the model tips $H3$, $T4$, dimer, $Si_{70}H_{50}$, $Si_{71}H_{50}$, $Si_{72}H_{50}$, $Si_{238}H_{118}$, $Si_{50}/Si(001)$.

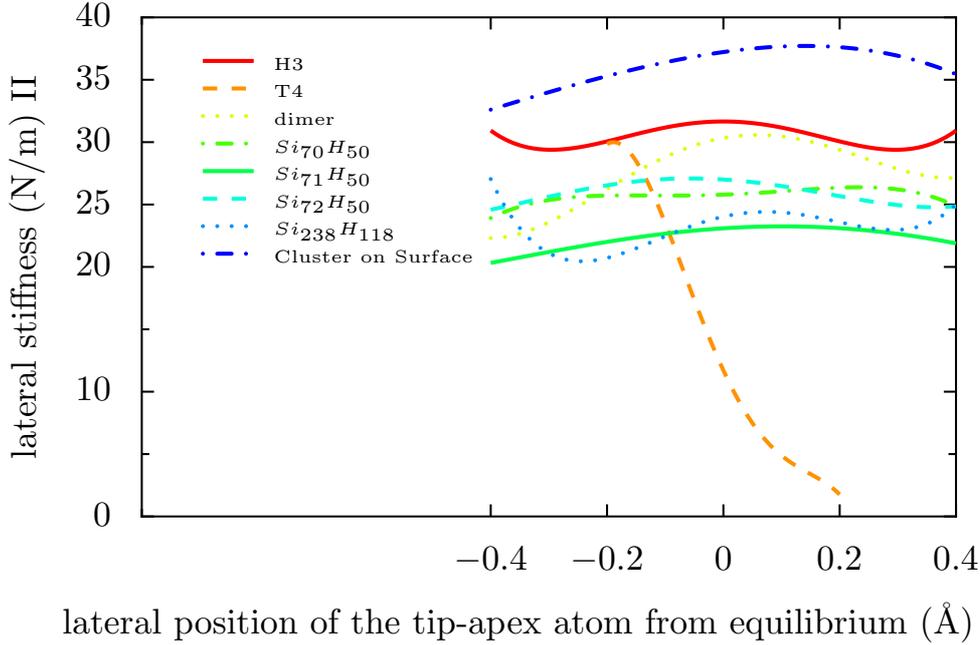


Figure 3.18: The lateral stiffness II of the model tips $H3$, $T4$, dimer, $Si_{70}H_{50}$, $Si_{71}H_{50}$, $Si_{72}H_{50}$, $Si_{238}H_{118}$, $Si_{50}/Si(001)$.

3.3.8 Discussion

The structural features of the medium-sized silicon model tips are different for $Si_{70}H_{50}$, $Si_{71}H_{50}$ and $Si_{72}H_{50}$. The lowest energy configuration of the $Si_{70}H_{50}$ is rather blunt, that of $Si_{71}H_{50}$ sharp, that is one atom protrudes more, and, that of $Si_{72}H_{50}$ is also fairly blunt. Nevertheless, there are many configurations with a sharp apex among the metastable configurations of $Si_{70}H_{50}$ and $Si_{72}H_{50}$. However, there are very few apex structures with T4-like configurations. From the thermodynamical point of view, the lowest energy configuration is important at low temperatures. On the other hand, at room temperature T_R other low-energy configurations are partially occupied according to the Boltzmann distribution $\exp(-E/K_B T)$, provided the system is ergodic. At RT, $K_B T_R \approx 0.025\text{eV} \approx 1\text{mHa}$, therefore, a configuration with an energy around $0.1\text{eV} \approx 4K_B T_R$ higher than the lowest one would on average be occupied during 0.02 fraction of the time compared to the lowest one. A recent MHM investigation on small and medium size silicon clusters by Hellmann and coworkers in Refs. [79, 80, 81] revealed the existence of low-energy isomers which are energetically very close to the ground state. Their results were obtained by density functional theory calculations, also partially supported by Quantum Monte Carlo (QMC) calculations. As a consequence, entropy effects can play an important role in defining the alternative stable structures taking into account that at room temperature the most stable structure has lowest free energy, rather than the lowest internal energy. Unfortunately, our realistic model tips are larger than clusters which nevertheless can at present be simulated by DFT or QMC. These highly reliable calculations on all of the

Si model tips lead to qualitatively similar results, i.e. for all of the model tips $Si_{70}H_{50}$, $Si_{71}H_{50}$, $Si_{72}H_{50}$, $Si_{238}H_{118}$ and Si_{50} on the reconstructed Si(001) surface there are always several low-lying energy structures. This can not be an artifact of the approximate tight-binding scheme, but is rather a general property of such frustrated covalently-bonded systems. The lowest energy structures of the model tips obtained by MHM are softer than the small model tips namely H3, T4 and dimer, which were used previously in the simulations of NCAFM. On average our model tips are softer by a factor of two. Moreover, our model tips are not as soft as real Si tips. On the other hand, all of our model tips show consistent values and small variations of the stiffness in contrast to the small model tips. By using a more realistic model tip such as the model tips presented in this chapter, one has a better chance to obtain novel results, e.g. we could reveal a new mechanism of the energy dissipation occurring in NCAFM experiments at room temperature which use a Si tip as the probe. These results are discussed in detail in the next chapter. In fact such hitherto unknown processes are relevant to friction, dissipation, etc. on the atomic-scale which are currently of high interest. For instance, dissipation of force *hysteresis* is discussed in detail in the literature but has mainly attributed to surface processes. However our results indicate that the tip can mainly be responsible for such processes in an AFM experiment. This is also discussed in detail in the next chapter.

Due to the routinely obtained atomic-scale resolution in noncontact atomic force microscopy experiments it is widely accepted that one atom at the tip-apex should protrude, this is in fact true in most of the low energy structures obtained by MHM. The other blunter apex structures can dynamically become sharp. However, in the third chapter of this dissertation attention is focussed on dissipation arising from the sharp structures.

3.3.9 Conclusion

In summary, we have provided a more realistic atomistic description of silicon tip apexes used in the AFM experiments with atomic resolution. We performed calculations of several model systems using several methodologies to make a systematic investigation of possible tip apexes. The results show that there are several types of atomically sharp terminations - the T4, H3 or dimer structures introduced in previous studies [66, 68, 67, 64, 65]. Furthermore, our results show that configuration of the tip last atomic layers could be both amorphous or crystalline.

Chapter 4

Ubiquitous Mechanisms of Energy Dissipation in Noncontact Atomic Force Microscopy

4.1 Introduction

In most dynamic force microscopy experiments, a microfabricated high-Q silicon cantilever is driven in ultrahigh vacuum at its fundamental flexural resonance. Using the frequency-modulation operation mode (FM-AFM), atomic resolution in the attractive force range has been routinely achieved on a variety of surfaces [132, 101, 102, 103]. In this mode, during imaging, the cantilever is usually kept oscillating with a constant amplitude at the resonance frequency of the cantilever. The resonance frequency is shifted by the tip-sample interaction, which is a function of the distance between the tip and the sample. The tip apex thus senses interaction with surface atoms at its turning point near the sample. The force on the tip can be determined from the frequency shift, and thus provides insight into short-range interactions at different sites and thus into mechanisms producing atomic-scale contrast.

Experimental observations reveal genuine interaction-induced energy dissipation of the order of 0.1 to a few eV per cycle [104, 105, 124, 127]. Two apparently distinct dissipation mechanisms of mechanical origin have been proposed [107]. Energy dissipation in AFM experiments has mainly been attributed to atomic jumps between the tip and the surface or to instabilities in the upper surface layers. The stochastic damping mechanism relates dissipation to the Brownian motion of atoms [108].

Values in the experimental range are, however, predicted by the former atomic adhesion hysteresis mechanism [135, 109] which postulates that an atom hopping back and forth between tip and sample leads to a force difference between approach and retraction in

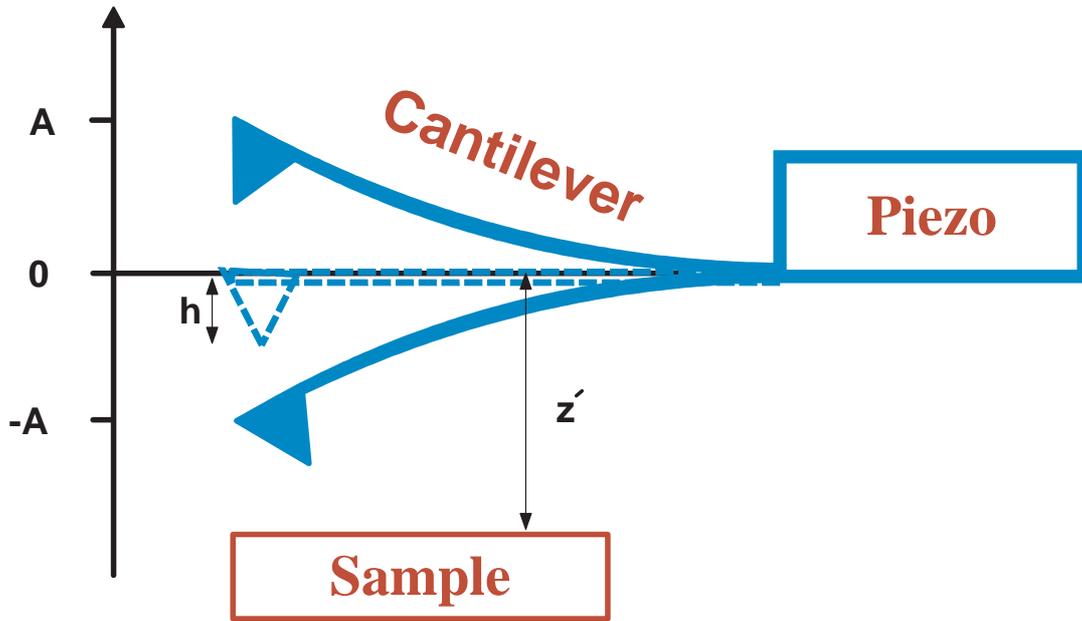


Figure 4.1: Schematic of the cantilever oscillating next to a sample.

each oscillation cycle. The area enclosed by the resulting hysteresis loop yields the energy dissipated per cycle. With typically used cantilever oscillation amplitudes of a few nanometers, the two different forces cannot be extracted because the measured frequency shift only senses the average tip-sample interaction in the two states. Actually, the transition between the stochastic damping and hysteresis regimes can be somewhat smeared by thermal fluctuations, as demonstrated in simulations [73, 110, 129]. In a different approach [105], using a sub-Å amplitude at a constant frequencies well below the first flexural resonance, in this mode the AFM response is linear. This makes possible direct quantitative measurements of the force gradient possible but this advantage is offset by the considerably higher sensitivity of FM-AFM on resonance.

Based on a Langevin equation approach, a scheme referred to as noncontact dissipation force microscopy (NC-DFM) was proposed in Ref. [108] which can be used for producing surface images in UHV. This model is elaborated and the importance of a consistent non-equilibrium consideration is stressed in Ref. [109]. At largest separations the potential is found to be conservative, as might be expected, but at smaller separations the interaction can become hysteretic [104, 105, 127, 106]. Atomic scale contrast dissipation images has in fact been obtained at low and room temperature [106]. Using molecular dynamics with Langevin boundary condition [112], it was shown that the stochastic energy dissipation in noncontact atomic force microscopy is several orders of magnitude smaller than the measured energy dissipation and therefore does not contribute to atomic scale contrast. Some calculations Refs. [113, 110, 129] demonstrate the existence of a link between dissipation hysteresis and the existence of a soft vibrational mode on the surface either introduced or induced by the presence of the tip.

In Ref. [126] R. Hoffmann and coworkers have shown that jumps in the frequency shift correlated with a rise in energy dissipation below a site-dependent distance can be traced back to rare hopping events close to the apex of the SFM tip. They have proposed that a KBr molecule executing specific hops near the corner of a small KBr cluster picked from the sample might explain the low energy barrier and distance-dependent asymmetry underlying such phenomena of the double well potential.

In summary, studies published so far have considered mainly two different mechanisms of energy dissipation. Various authors have predicted *velocity dependent dissipation* [115, 116, 117, 118, 119, 108, 120, 121]. Viscous damping [115, 117, 118, 119], stochastic friction [108, 120], or van der Waals friction [121] are the assumed physical origins of this type of dissipation. Another idea is that dissipation is due to *hysteresis* effects caused by different tip-sample forces during approach and retraction even in case of zero velocity [115, 118, 119, 135, 129]. Such a hysteresis might be caused by adhesion between tip and sample or by other bistabilities in the tip-sample contact [135, 129, 122, 123]. In fact a thorough dynamic force spectroscopy investigation of the energy dissipation [114] on graphite (0001) using Si tips in vacuum in the attractive and repulsive regime showed that the energy dissipation is not velocity dependent and must therefore be caused by hysteresis.

Existing models cannot, however, explain the following facts: First, energy dissipation has been observed in many NCAFM experiments with atomic resolution on different samples. Second, dissipation images often exhibit sudden contrast changes while simultaneously recorded topography images are much less affected. Thus dissipation in NCAFM sensitively depends on the "tip state" in an hitherto poorly understood fashion [127]. Our work explains these ubiquitous features and thus contributes to the general understanding of tip-induced dissipation processes in atomic-scale scanning probe investigations.

4.2 Investigating Energy Dissipation in NCAFM Using More Realistic Model Tips

Having obtained and characterized more realistic model tips in chapter three, we used the tip structures presented in section 3.3.4 in atomistic simulations which revealed novel dissipation mechanisms in non-contact atomic force microscopy. The potential energy surfaces of realistic silicon tips exhibit many energetically close local minima that correspond to different structures. Most of them easily deform, thus causing dissipation arising from hysteresis in force vs. distance characteristics. Furthermore, saddle points which connect local minima can suddenly switch to connect different minima. Configurations driven into metastability by the tip motion can thus suddenly access lower energy structures when thermal activation becomes allowed within the time required to detect the resulting average dissipation.

Atomic resolution of surface features is achieved if the sharp tip at the cantilever end comes within the range of short-range chemical and/or steric interactions with the sample. The total tip-sample interaction causes a frequency shift Δf which can be kept constant in order to record a topographic image. The average energy ΔE dissipated per cycle arising from nonadiabatic relaxation processes induced by time-dependent tip-sample forces can be simultaneously measured [124]. The net work done per cycle by the cantilever oscillating perpendicular to the surface is given by

$$W = - \oint F(z) dz, \quad (4.1)$$

where the integral is taken over one oscillation, $z = z' - h$ (z' and h are specified in the Fig. 4.1) is the vertical distance between the outermost atoms of the tip and the surface, ignoring relaxation effects, while $F(z)$ is the z -component of the force acting on the tip, including those effects. This is reasonable because z tracks the motion of the cantilever end, while changes in $F(z)$ are typically transmitted within ~ 1 ns through the tip. Possible dissipation mechanisms have been reviewed [127]; typical values of $\Delta E \sim 0.1 - 1$ eV per cycle have been observed under stable imaging conditions. They can be attributed to one or a few sample atoms rapidly jumping back and forth upon tip approach and retraction below a site-dependent critical distance z_c . At zero temperature, a jump $\Delta V_i < 0$ occurs in the potential energy $V(z)$ of the tip-sample system whenever the system rearranges. The current potential minimum then disappears together with the energy barrier (a saddle point in configuration space) separating it from another lower minimum. Because $F(z) = -\partial V/\partial z$ between successive jumps, Eq. (4.1) implies that $W = -\sum_i \Delta V_i$. The energy released at each jump i excites vibrations which eventually decay, i.e. energy is dissipated. Energy conservation implies $\Delta E = W$ on average. Typical vibrational relaxation times being less than 1 ns, jumps can be considered as instantaneous. They lead to a hysteretic force $F(z)$ in each cycle and, at zero bath temperature, to a step in Δf and to a stepwise increase of ΔE at z_c [135]. At finite temperature, such jumps can be thermally activated before the relevant barrier disappears, i. e. slightly above z_c . The hysteresis is thereby reduced, and the steps in Δf and ΔE are smeared on average [129]. The finite response times of the measurement electronics lead to similar effects [136].

Recent atomistic simulations have focused on jumps of sample atoms induced by the tip on (001) cleavage planes of ionic crystals [136, 137, 141] or on reconstructed Si and Ge surfaces [131, 128, 67, 69]. However these simulations assumed rather small MgO or Si clusters as model tips. Energy dissipation then arises from instabilities in the positions of sample atoms subjected to short-range interactions. Such scenarios require a particular combination of tip and sample properties and therefore cannot explain dissipation in general. In the following we show that relaxation and rearrangements within more realistic silicon tips can also lead to hysteresis, hence additional dissipation. This mechanism is active on almost any sample. In order to study these effects, we selected more than

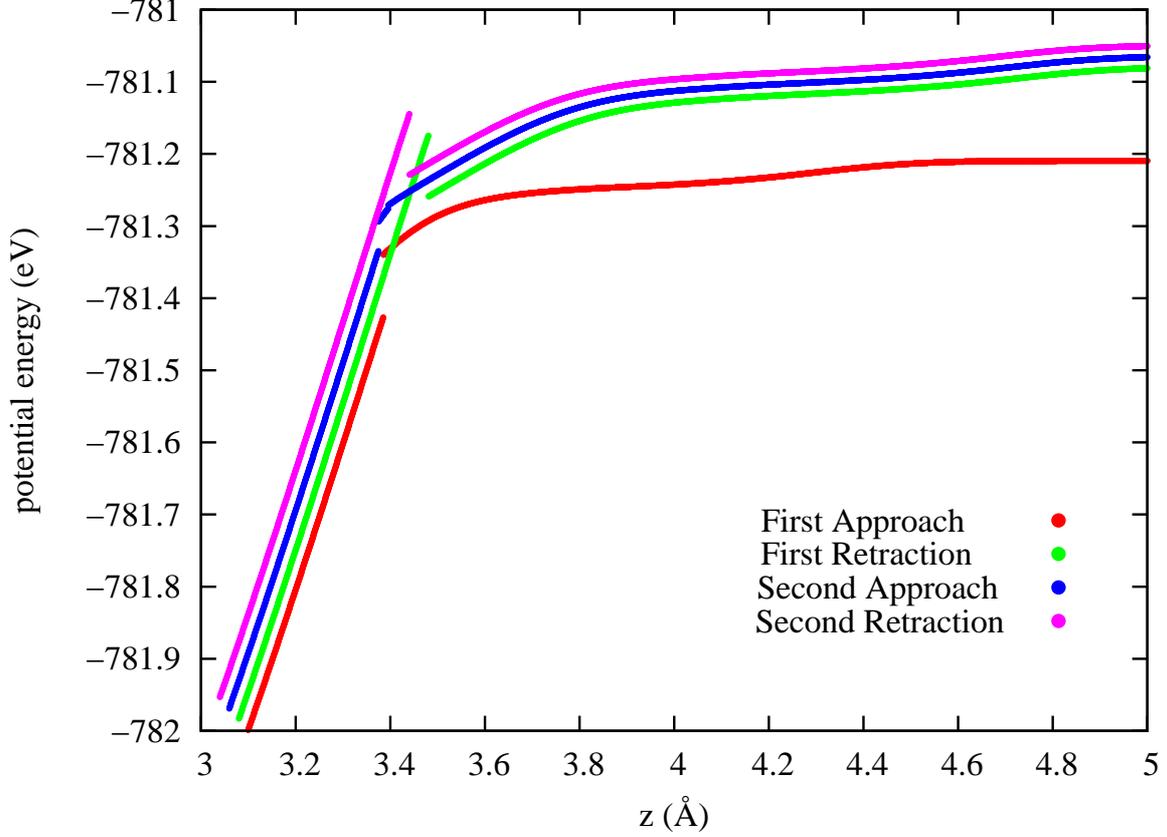


Figure 4.2: Potential energy vs. unrelaxed tip-sample distance z for two subsequent approaches and retractions. The first retraction and the second cycle curves are slightly shifted to the left (by steps of 0.02 Å) and upwards (by steps of 0.015 eV) to clarify the figure.

thirty low-energy configurations, out of several thousand structures of model $Si_{72}H_{50}$ tips generated by the minima hopping algorithm [91], for a more detailed study. Then we computed their total energies $V(z)$ in a few quasi-static approach-retraction cycles of the tip down to $z = 3.1$ Å above the up atom of a tilted dimer on the pre-relaxed $p(2 \times 1)$ reconstructed (001) surface of a slab with all Si atoms fixed. Twenty five silicon atoms near the tip apex were allowed to relax, whereas atoms in the base of the tip were kept fixed. This allows comparison with simulations of the same system, which assumed a small $Si_{10}H_{15}$ tip but allowed relaxation of surface layers [131, 128]. Our computations were performed with a tight-binding model, encompassing the Lenosky tight-binding parameters for Si [77], together with additional parameters fitted using a similar methodology to accurately model Si-H and H-H interactions relevant for hydrogen terminated surfaces and clusters.

In practice a sharp reactive silicon tip obtained, e.g. by sputtering off the native oxide, exposes many atoms that cannot be in the preferred fourfold coordination environment. A large number of distorted structures have very similar energies. Six tip structures

with energies within an interval of 0.1 eV, are displayed in Fig. 3.7. In the case of free Si_N clusters ($N \geq 13$), similar small energy differences have also been found in density functional or even more accurate Quantum Monte Carlo calculations [80, 81]. This is thus certainly not an artifact of the tight-binding scheme, but a general property of such frustrated covalently-bonded systems.

Our model tips have a fixed crystalline base which enforces a pyramidal shape. However, several threefold coordinated atoms with dangling bonds, themselves bonded to threefold or fourfold coordinated atoms with strained bonds and bond angles invariably occur around the apex. Tips with one protruding atom facing an up dimer atom produce $V(z)$ curves with one downward jump upon approach and retraction, respectively, without transfer of atoms in the investigated range. However, as shown in Fig. 4.2, the initial cycle is sometimes different from subsequent ones. This implies a dynamical stabilization of certain tip configurations. In most runs, this stabilization is established from the start. An example is shown in Fig. 4.3. Corresponding values of ΔE ranged between 0 and about 0.5 eV per cycle. By contrast, in a previous study a unique $F(z)$ was found with a small adatom-terminated Si tip above an up dimer atom on the $c(4 \times 2)$ Si(001) surface, whereas a hysteretic $F(z)$ leading to $\Delta E = 0.3$ eV was found above a down dimer atom [131, 128]. In those studies the main contribution to ΔE was attributed to dimer flipping on the surface, while it is solely due to tip deformation in our case. A semiquantitative comparison between both studies appears justified. Indeed, both the dimer flip in Ref. [131, 128] and the tip deformation in our case are triggered by bond formation between the outermost tip atom and the nearest surface atom. The maximum attractive force was -2.75 nN at $z = 3.2$ Å in the former computation [131], compared to -3.4 ± 0.2 nN at 3.3 ± 0.1 Å achieved on the nearly linear $V(z)$ branch which appears at short distances in our stabilized cycles.

By analogy with the behavior of a soft cantilever subject to adhesive forces, the observed jumps (which occur whenever the force gradient exceeds the stiffness of the tip) are larger if the tip is softer. The large spread in tip stiffness, hence in ΔE , arises because of the above-mentioned differences in the coordination of back-bonded atoms and of the resulting strains in the amorphous-like apex structure. We surmise that if surface dimer relaxation were allowed, ΔE would still be dominated by tip deformation, at least for the softest tip structures.

Let us next discuss effects due to a finite temperature T . As already pointed out and discussed in detail for sample atoms displaced by the tip [69, 129, 128, 136, 137, 141, 131, 67], thermal activation over energy barriers which vanish at the end points of $V(z)$ branches like those in Figs. 4.2 and 4.3 allow highly non-equilibrium populations of those branches to relax into populations that are closer to thermal equilibrium. The importance of such effects can be assessed by comparing the mean residence times in local energy minima with time scales relevant in NCAFM experiments [127, 136, 141, 133]. Transition state theory [138] predicts a mean jump rate out of a local energy minimum of

$$\nu = \nu_0 \exp(-E_a/(k_B T)), \quad (4.2)$$

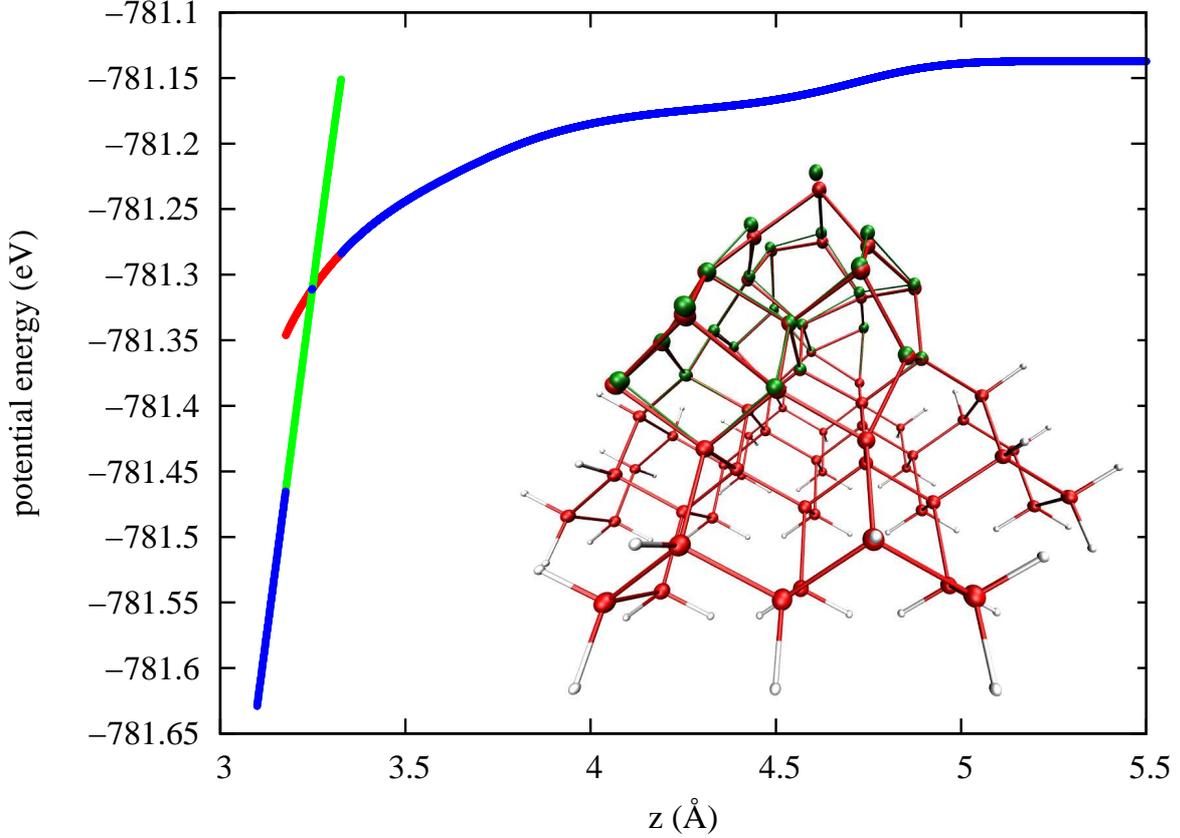


Figure 4.3: Representative $V(z)$ variation for a stable set of tip structures. Inset: structures corresponding to the two configurations near the crossing. (red: approaches, green: retractions, blue: coinciding segments)

where E_a is the energy barrier to be surmounted and the attempt frequency ν_0 is roughly 10^{13} Hz. The following estimates refer to room temperature (RT), but can be scaled if desired using Eq. (4.2). One relevant scale is determined by the time during which the tip can strongly interact with a surface atom. Our simulations, as well as previous ones, show that this occurs within a range $d \sim 1$ Å around the turning point of the tip. For a typical oscillation amplitude $A \sim 100$ Å at a frequency $f \sim 100$ kHz, the "interaction time" is $\sqrt{(d/A)}/f \sim 10^{-6}$ s. Within this time barriers of up to 0.41 eV can be surmounted. The corresponding threshold would be 0.45 eV if a whole oscillation period were considered. Another relevant scale is the response time of the amplitude controller over which dissipation is effectively sampled (at least $\sim 10^{-3}$ s). Within this interval 0.58 eV barrier could be surmounted, leading to a hysteresis loop in one out of 100 cycles and a 100 times lower average dissipation. To reduce noise, measurements are made at closely spaced positions over an averaging time t_{av} of up to 0.1 s; dissipation arising from jumps over barriers less than 0.70 eV could then be measured. On the other hand, individual jumps over higher barriers would be detectable in real time, either as telegraph-like noise [126] or as sudden changes in image contrast [136, 141, 69]. Hereafter,

attention is focused on situations where only continuous dissipation is measured.

Barriers to flip a single dimer were estimated to be 0.12 and 0.20 eV for the p(2 x 1) and c(4 x 2) reconstructions of the Si(001) surface, respectively [128], and similar barrier heights are expected for the dimer-like configurations at the surfaces of our tip structures. Deeper inside the tip, barriers existing for amorphous silicon may be more appropriate. Starting from well-relaxed configurations of that material, an extensive search yielded a 2.4 eV wide distribution of the lowest barriers with a maximum around 3 eV extending down to zero [71]. Judging from Fig. 2 and estimates in that work, roughly one energy barrier below 0.5 eV per relaxed atom is expected.

Owing to interaction with the surface, the energies of all tip structures vary as a function of z (see Fig. 4.2), hence time. Moreover, energy differences between different tip configurations also change and the corresponding $V(z)$ curves can even cross. The lowest energy barriers connecting those configurations also vary. Using an "improved dimer method" [125], we initiated searches for the lowest barriers connecting a few of our low-energy tip structures to other structures as a function of decreasing z . In the process we found many barriers, several ones between 0.4 and 0.7 eV, for distances somewhat larger than z_c . Thus activated transitions between different tip structures can occur at RT even before the $V(z)$ branch corresponding to bond formation is reached. Moreover, during the tip motion, the same saddle point can suddenly connect one of the two connected minima to a different one or even connect a new pair of local minima. Such a switching of the connectivity can occur if the energy landscape of a complex system [139] is qualitatively changed by an applied bias, e.g. the tip-sample interaction in our case. Changes in connectivity thus happen at distances where the tip-sample interaction is weaker than that needed for a minimum to disappear.

If all barriers were significantly smaller than 0.4 eV, configurations corresponding to different local minima would be maintained in thermal equilibrium by frequent jumps during each cycle, and negligible dissipation would occur. By analogy with reacting chemical species (see, for instance, [140], it would then be sufficient to replace $V(z)$ by the free energy, i.e. a sum over stable tip structures weighted by Boltzmann population factors times local vibrational free energies. If weights < 0.01 are considered negligible, only structures with energies differing by less than 0.12 eV need be considered. If all saddle points connecting those local minima were higher than 0.7 eV, then their populations would essentially be frozen over t_{av} , and dissipation would again be negligible.

Dissipation occurs if some of the barriers lie between 0.4 and 0.7 eV. We then consider groups of local minima instead of individual minima. The minima within each group remain in local equilibrium if they are connected by barriers much less than 0.4 eV. The motion of the tip continuously changes the free energy of each group and drives certain groups into metastability if they are surrounded by high barriers. Dissipation occurs whenever such a group can suddenly relax into other lower free energy groups. Such an event becomes probable if under a certain tip-sample distance either a barrier

connecting two groups continuously drops below 0.7 eV or if a new lower barrier suddenly appears due to a connectivity change. Our simulations suggest that the latter mechanism is statistically more frequent. Saddle points and their connectivity are more sensitive to the tip-sample interaction than local minima.

We expect that groups of tip configurations which are in thermal equilibrium will also stabilize dynamically at finite temperature for distances of closest approach below or near z_c . In contrast to the $T = 0$ case, the tip structure will switch between different configurations during t_{av} . There is no well defined tip structure, as was assumed in previous work. At $T = 0$, ΔE was found to vary between 0 and 0.5 eV, depending on which tip structure is stabilized dynamically. At finite temperature, those variations will tend to average out over the sampled cycles. Taking a simple average over computed stabilized cycles like in Fig. 4.3, a rough estimate $\Delta E \approx 0.27$ eV is obtained.

4.3 Conclusion

In summary, non-equilibrium processes within silicon tips used in near-contact AFM are expected to dominate energy dissipation induced by short-range interactions with the sample. The softness of the frustrated apex structures facilitates hysteretic atomic rearrangements of tip atoms; this results in dissipation. Thermally activated jumps between temporarily equilibrated groups of tip configurations cause an intermittent redistribution of their populations and sudden energy losses which are, however, averaged over the time required to detect the dissipation. Stable, though somewhat noisy atomically-resolved images of topography and dissipation can then be simultaneously recorded in a limited range of temperature and distance z , as noticed in the case of diffusing surface species [137, 141]. The phenomena discussed occur if short-range interactions are sufficiently strong to locally modify the potential energy landscape of the tip-sample system and will in general be sample-specific as well.

Chapter 5

Conclusions and Outlook

In the work reported in this thesis we mainly focused on two issues which are of importance to simulations of atomic force microscopy. First, the development of methods which have proven to be crucial tools performing the appropriate atomistic simulations. Second: the recognition of fundamental features of experimental importance in atomic force microscopy based on atomistic simulations. In the following, we summarize the developed methods and acquired results.

In chapter two, the P^3S and the P^3D methods are introduced and discussed in detail including test results which validate our implementation of both methods. The P^3S method calculates the Coulomb interaction for three dimensional free boundary conditions. In contrast to most available methods, it intrinsically preserves the free boundary condition. It also scales $\mathcal{O}(N \log N)$ N being the number of particles, with a small prefactor. Furthermore, energy, in contrast so some other methods, is accurately conserved due to the fact that the approximate forces are exact analytical derivatives of the approximate energy. The use of wavelet theory to calculate the long-range part of the energy corresponding to the electrostatic energy of a collection of smooth Gaussian charge distributions is a novel approach which is elaborated in the P^3S method. This method is an excellent technique which can be used in simulations of large ionic clusters ($N > 1000$), e.g. to investigate possible structures of an ionic nanotip.

The P^3D method is also introduced and discussed in detail in chapter two. As a matter of fact it does a remarkable job in calculations of the Coulomb interaction with surface boundary conditions. Its main new feature is that it uses a mixture of two basis sets, plane waves and finite elements, parallel and perpendicular to the surface, respectively. This technique is ideally suitable for surface problems and can be used in many simulations of systems with slablike geometry whenever the Coulomb interaction is involved. This technique is not suitable for other type of boundary conditions, but is superior to other existing methods to calculate the Coulomb interaction with surface boundary condition. It scales linearly with respect to the number of particles, and also preserves this boundary

conditions intrinsically. Furthermore, the error is distributed uniformly throughout the simulation box. In addition, molecular dynamics simulation on a sodium chloride system over a relatively long time (8 nanoseconds) shows that the energy is conserved. An interesting aspect of this method is that it is not based on a sophisticated theory, one only needs to be familiar with finite element methods and fast Fourier transforms, which can be found in many textbooks.

In chapter three, we mentioned the Si-H tight-binding scheme developed by us which is a generalization of the Lenosky Si tight-binding scheme in order to include the Si-H and H-H interactions. It was then used in a systematic search of possible Si tip-apex structures. Several different partially constrained H-passivated Si clusters of different sizes as well as a cluster on a silicon surface were investigated by the minima hopping method (a systematic global optimization method which searches for the low lying energy structures with the goal of finding the global minimum). Our results for both medium and large model tips show that for each one there are several structures which only slightly differ in energy with respect to the lowest one, such that from the thermodynamical point of view they can be significantly occupied at room temperature. A similar behavior is observed for the cluster on the Si surface with the difference that the low energy structures for this model tip differ from each other at the surface while for the other investigated model tips the tip-apex structures of the low energy configurations differ drastically in most cases. Model tips, both blunt and sharp structures have been obtained among the low energy structures. These results indicate that assuming a single structure to be the candidate tip-apex structure is not acceptable. As a consequence, one should consider an average, with proper weights (not necessarily Boltzmann factors) which correspond to the near-equilibrium behavior of the tip dynamics, of the structures which can be occupied in the experimental measurement time scale. In the last section of chapter three, the vertical and lateral stiffnesses of all the model tips (including ours and smaller ones considered earlier by others), as the tip-apex atom (the foremost atom) is pulled or pushed, were calculated. From experiments one knows that Si tip-apex can be quite soft, that even our model tips can not reproduce such softness. However, this fact is less important than the interesting feature of our model tips the nearly constant stiffness. In contrast to the smaller model tips which exhibit quite nonlinear anisotropic and asymmetric stiffnesses for apex displacements of $\pm 0.4 \text{ \AA}$.

In chapter 4, inspired by low lying energy structures which are a consequence of the intricate energy landscape of frustrated Si systems, we believed that the energy dissipation occurring in almost all atomic force microscopy experiments must arise from the tip as well as from the surface. This fact has not been seriously taken so far. In our investigation, we mainly paid attention to atomic instabilities within the tip itself as an additional source of the energy dissipation in the dynamic atomic force microscopy. We made a valid point that the actual tip may be very far from being simply ripped off the crystalline sample as it is usually implied in actual simulations. Instead, there could be a possible large number of tip structures all with very similar energies and a wide spectrum of barriers separating

them. Another interesting result is that the tip structure may require some number of oscillation cycles to become stable. Furthermore, during tip approach or retraction, the tip structure may change as well, even a small variation of the interaction with the surface may cause a change of “connectivity” between energy minima, so that the energy barriers (in fact, the whole energy landscape) could switch depending on the tip position above the surface. Finally, the complex issue of temperature dependence is discussed in the context of complicated energy landscapes. We expect that our original work on energy dissipation will stimulate a series of studies aimed at a better understanding of the role played by tip itself in dissipation images recorded during the atomic force microscopy.

Appendix A

The Details of the System of Linear Equations for the P^3D Method.

We consider a uniform grid on the interval $[z_l, z_u]$ with $N + 1$ nodes $\{z_0, z_1, \dots, z_N\}$ where $z_0 = z_l$ and $z_N = z_u$. The interval is thus divided into N equally spaced subintervals(elements). The functions $d(z)$ and $c(z)$ are replaced by the approximate functions $D(z)$ and $C(z)$ which are expanded in the basis of Eqs. (2.31) on each subinterval. We use the Galerkin approach in which the same basis is used for the expansion of both $D(z)$ and $C(z)$. Our basis consists of the hat function $\phi^v(z)$ centered at the nodes

$$\phi_j^v(z) = \begin{cases} (z_{j+1} - z)/h, & z \in [z_j, z_{j+1}) \\ (z - z_{j-1})/h, & z \in [z_{j-1}, z_j) \\ 0 & \text{otherwise} \end{cases} \quad (\text{A.1})$$

$$(\text{A.2})$$

and of the hierarchical polynomials[58] $\phi^m(z)$

$$\phi_{j,i}^m(z) = \begin{cases} N_i(2^{\frac{z-z_j}{h}} + 1), & z \in [z_{j-1}, z_j] \\ 0 & \text{otherwise} \end{cases} \quad (\text{A.3})$$

which are localized within the individual elements. N_i are given in canonical coordinates in Eqs. (2.31). Finally $C(z)$ and $D(z)$ within the element $[z_{j-1}, z_j]$ are:

$$C(z) = c_{j-1}\phi_{j-1}^v(z) + c_j\phi_j^v(z) + \sum_{i=2}^p c_{j,i}\phi_{j,i}^m(z) \quad (\text{A.4a})$$

$$D(z) = d_{j-1}\phi_{j-1}^v(z) + d_j\phi_j^v(z) + \sum_{i=2}^p d_{j,i}\phi_{j,i}^m(z) \quad (\text{A.4b})$$

Because $\phi_{j,i}^m(z)$ vanishes at all nodes $c_j = C(z_j)$. Substituting the approximate functions from Eq.(A.4a) and Eq.(A.4b) into equation (2.36) gives

$$\sum_{j=1}^N [A_j(D, C) - (D, \eta)_j] = gd_0c_0 + gd_Nc_N \quad (\text{A.5})$$

We split $A_j(D, C)$ as

$$A_j(D, C) = A_j^S(D, C) + A_j^M(D, C) \quad (\text{A.6})$$

where

$$A_j^S(D, C) := - \int_{z_{j-1}}^{z_j} D'(z)C'(z)dz \quad (\text{A.7})$$

$$A_j^M(D, C) := - \int_{z_{j-1}}^{z_j} g^2 D(z)C(z)dz \quad (\text{A.8})$$

$$(D, \eta)_j := \int_{z_{j-1}}^{z_j} D(z)\eta(z)dz \quad (\text{A.9})$$

$C(z)$ within an element is:

$$C(z) = \vec{\phi}_j^T(z)\vec{c}_j \quad z \in [z_{j-1}, z_j] \quad (\text{A.10})$$

where \vec{c}_j and $\vec{\phi}_j(z)$ are vectors with $p + 1$ elements:

$$\vec{c}_j := [c_{j-1}, c_j, c_{j,2}, \dots, c_{j,p}]^T \quad (\text{A.11})$$

$$\vec{\phi}_j(z) := [\phi_{j-1}^v(z), \phi_j^v(z), \phi_{j,2}^m(z), \dots, \phi_{j,p}^m(z)]^T \quad (\text{A.12})$$

Then

$$A_j^S(D, C) = \vec{d}_j^T K_j \vec{c}_j \quad (\text{A.13})$$

$$A_j^M(D, C) = \vec{d}_j^T M_j \vec{c}_j \quad (\text{A.14})$$

where

$$K_j := - \int_{z_{i-1}}^{z_i} \frac{d\vec{\phi}_j}{dz} \frac{d\vec{\phi}_j^T}{dz} \quad (\text{A.15})$$

$$M_j := - \int_{z_{i-1}}^{z_i} g^2 \vec{\phi}_j \vec{\phi}_j^T \quad (\text{A.16})$$

By analogy with continuum elasticity theory, the $(p + 1) \times (p + 1)$ matrix K_j is called the element stiffness matrix and the $(p + 1) \times (p + 1)$ matrix M_j is called the element mass matrix. Although the element index j is present in the definition of K_j and M_j , in

our case of uniform grid spacing these matrices do not depend on j . By performing the summation $\sum_{j=1}^N A_j^M$ and $\sum_{j=1}^N A_j^S$, we build up the global mass matrix and the global stiffness matrix. We arrange the order of elements of these matrices as:

$$\vec{c} := \begin{bmatrix} \vec{c}_L \\ \vec{c}_Q \end{bmatrix} \quad (\text{A.17})$$

$$\vec{c}_L := [c_0, c_1, \dots, c_N]^T \quad (\text{A.18})$$

$$\vec{c}_Q := [c_{1,2}, \dots, c_{1,p}, \dots, c_{N,2}, \dots, c_{N,p}]^T \quad (\text{A.19})$$

$$K = \begin{bmatrix} K_L & 0 \\ 0 & K_Q \end{bmatrix} \quad (\text{A.20})$$

$$M = \begin{bmatrix} M_L & M_{LQ} \\ M_{LQ}^T & M_Q \end{bmatrix} \quad (\text{A.21})$$

The second term of the summand in Eq.(A.5) is calculated approximately because only the values of $\eta(z)$ on the nodes are available:

$$(D, \eta)_j = \vec{d}_j^T \vec{I}_j \quad (\text{A.22})$$

where

$$\vec{I}_j := \int_{z_{j-1}}^{z_j} \vec{\phi}_j(z) \eta(z) dz \quad (\text{A.23})$$

Interpolating integration is appropriate to calculate the above integral by fitting a polynomial of degree $d \geq 2p$ to the nodes of element $[z_{j-1}, z_j]$ and its neighboring nodes:

$$(\vec{I}_j)_i = \sum_{k=-p}^{p-1} w_k^i \eta_{j+k} \quad (\text{A.24})$$

Recall that our charge density is localized within the interval $[z_l, z_u]$ and it smoothly tends to zero at the edges. Therefore it is appropriate to zero pad the ends of the $\eta(z)$. The coefficients w_k^i are weights from high-order interpolation. Building up the global matrices yields:

$$(D, \eta) = \vec{d}^T \vec{I} \quad (\text{A.25})$$

where the elements of the vector \vec{d} are coefficients of expansion of test function $D(z)$ as denoted in Eq. (A.4a) and the order of elements of \vec{I} is the same as in Eq. (A.17),

$$\vec{I} := \begin{bmatrix} \vec{I}_L \\ \vec{I}_Q \end{bmatrix} \quad (\text{A.26})$$

$$\vec{I}_L := [I_0, I_1, \dots, I_N]^T \quad (\text{A.27})$$

$$\vec{I}_Q := [I_{1,2}, \dots, I_{1,p}, \dots, I_{N,2}, \dots, I_{N,p}]^T \quad (\text{A.28})$$

Finally by adding the right-hand-side of Eq.(A.5) to the global matrices yields:

$$\begin{bmatrix} P_L & M_{LQ} \\ M_{LQ}^T & P_Q \end{bmatrix} \begin{bmatrix} \vec{c}_L \\ \vec{c}_Q \end{bmatrix} = \begin{bmatrix} \vec{I}_L \\ \vec{I}_Q \end{bmatrix} \quad (\text{A.29})$$

where M_{LQ} is a sparse $(N + 1) \times N(p - 1)$ matrix,

$$P_Q := K_Q + M_Q \quad (\text{A.30})$$

is a $N(p - 1) \times N(p - 1)$ block-diagonal matrix,

$$P_L := K_L + M_L - ge_0e_0^T - ge_Ne_N^T \quad (\text{A.31})$$

is a tridiagonal $(N + 1) \times (N + 1)$ matrix, and

$$e_0 := [1, 0, \dots, 0]^T \quad (\text{A.32})$$

$$e_N := [0, \dots, 0, 1]^T \quad (\text{A.33})$$

Multiplying the matrix in Eq.(A.29) and eliminating \vec{c}_Q in the system of linear equations yields:

$$[P_L - M_{LQ}P_Q^{-1}M_{LQ}^T] \vec{c}_L = \vec{I}_L - M_{LQ}P_Q^{-1}\vec{I}_Q \quad (\text{A.34})$$

Finally we obtain our system of linear equations:

$$B\vec{c}_L = \vec{b} \quad (\text{A.35})$$

where the matrix B and the vector \vec{b} are

$$B := P_L - M_{LQ}P_Q^{-1}M_{LQ}^T \quad (\text{A.36})$$

$$\vec{b} := \vec{I}_L - M_{LQ}P_Q^{-1}\vec{I}_Q \quad (\text{A.37})$$

It turns out that in the general case the matrix B is symmetric tridiagonal of dimension $(N + 1) \times (N + 1)$. The proof for the tridiagonality of matrix B can be found in the context of block cyclic reduction[61]. Note that elements of the vector \vec{c}_L are the values of $C(z)$ at the grid points. Therefore by solving a system of linear equations, which has a tridiagonal matrix, we can find the values of $C(z)$ at the grid points. Instead of using finite element method, we could have used finite differences to solve Eq. (2.22). Although calculating the right-hand-side \vec{b} is computationally more expensive in our approach than in the finite difference method, the whole process of solving the system of linear equations is less expensive because the factorization of the tridiagonal matrix can be done fast.

Bibliography

- [1] G. Binnig and H. Rohrer, *Helvetica Physica Acta* **55**, 726 (1982).
- [2] G. Binnig, C. F. Quate and C. Gerber, *Phys. Rev. Lett.* **56**, 930 (1986).
- [3] Y. Martin, C. C. Williams, and H. K. Wickramasinghe, *J. Appl. Phys.* **61**, 4723 (1987).
- [4] T. R. Albrecht, P. Grütter, D. Horne, and D. Rugar, *J. Appl. Phys.* **69**, 668 (1991).
- [5] D. Anselmetti, R. Luthi, E. Meyer, T. Richmond, M. Dreier, J. E. Frommer and H.-J. Guntherodt, *Nanotechnology* **5**, 874 (1994).
- [6] C. Bustamante and D. Keller, *Physics Today* **48**, 32 (1995).
- [7] Clemens Möller, Mike Allen, Virgil Elings, Andreas Engel, and Daniel J. Müller, *Biophys. J.* **77**, 1150 (1999).
- [8] A. San Paulo and R. García, *Biophys. J.* **78**, 1599 (2000).
- [9] G. Reiter, G. Castelein, P. Hoerner, G. Riess, J.-U. Sommer and G. Floudas, *Eur. Phys. J. E* **2**, 319 (2000).
- [10] Y. Sugawara, M. Ohta, H. Ueyama, and S. Morita, *Science* **270**, 1646 (1995).
- [11] S. Kitamura and M. Iwatsuki, *Jpn. J. Appl. Phys.* **34**, L145 (1995).
- [12] S. W. de Leeuw and J. W. Perram and E. R. Smith, *Proc. R. Soc. Lond.*, **373**, 27 (1980).
- [13] D. Fincham, *Mol. Simul.*, **13**, 1 (1994).
- [14] K. Esselink, *Comput. Phys. Commun.*, **87**, 375 (1995).
- [15] Albert H. Widmann, David B. Adolf, *Comput. Phys. Commun.*, **107**, 167 (1997).
- [16] E. L. Pollock, Jim Glosli, *Comput. Phys. Commun.*, **95**, 93 (1996).
- [17] Abdulnour Y. Toukmaji, John A. Board Jr., *Comput. Phys. Commun.*, **95**, 73 (1996).

-
- [18] P. H. Hünenberger and J. A. McCammon, *Biophys. Chem.*, **78**, 69 (1999).
- [19] P. H. Hünenberger and J. A. McCammon, *J. Chem. Phys.*, **110**, 1856 (1999).
- [20] M. P. Allen and D.J. Tildesley, *Computer Simulation of Liquids*, (Clarendon, Oxford, 1987 Sec. 5.5).
- [21] D. York, A. Wlodawer, L. Pedersen and T. Darden, *Proc. Natl. Acad. Sci.*, **91**, 8715 (1994).
- [22] H. Schreiber and O. Steinhauser, *Biochemistry*, **31**, 5856 (1992).
- [23] J. S. Bader and D. Chandler, *J. Phys. Chem.*, **96**, 6423 (1992).
- [24] M. Patra, M. Karttunen, M. T. Hyvönen, E. Falck and Ilpo Vattulainen, *J. Phys. Chem. B*, **108**, 4485 (2004).
- [25] M. Patra, M. Karttunen, M. T. Hyvonen, E. Falck, P. Lindqvist, and I. Vattulainen, *Biophys. J.*, **84**, 3636 (2003).
- [26] C. Anézo, A. H. de Vries, H.-D. Höltje, D. P. Tieleman, and S.-J. Marrink, *J. Phys. Chem. B*, **107**, 9424 (2003).
- [27] C. L. Brooks III, B. M. Pettitt, and M. Karplus, *J. Chem. Phys.*, **83**, 5897 (1985).
- [28] C. L. Brooks III, *J. Chem. Phys.*, **86**, 5156 (1987).
- [29] S. Kuwajima and A. Warshel, *J. Chem. Phys.*, **89**, 3751 (1988).
- [30] J. Shimada, H. Kaneko, and T. Takada, *J. Comput. Chem.*, **14**, 867 (1993).
- [31] U. Essmann, L. Perera, and M. L. Berkowitz, *J. Chem. Phys.*, **103**, 8577 (1995).
- [32] J. Lekner, *Physica A*, **176**, 485 (1991).
- [33] R. Strebler and R. Sperb, *Mol. Simul.* **27**, 61 (2001).
- [34] A. Neelov, S. A. Ghasemi, and S. Goedecker, *J. Chem. Phys.*, **127**, 024109 (2007).
- [35] L. Genovese, T. Deutsch, A. Neelov, S. Goedecker, and G. Beylkin, *J. Chem. Phys.*, **125**, 074105 (2006).
- [36] S. Goedecker, *Wavelets and their application for the solution of partial differential equations in physics* (Presses Polytechniques Universitaires et Romandes, Lausanne, Switzerland, 1998).
- [37] M. P. Tosi and F. G. Fumi, *J. Phys. Chem. Solids*, **25**, 45 (1964).
- [38] P. P. Ewald, *Ann. Phys. (Leipzig)*, **64**, 253 (1921).

-
- [39] L. Greengard and V. Rokhlin, *J. Comp. Phys.*, **73**, 325 (1987).
- [40] R. W. Hockney and J. W. Eastwood, *Computer Simulation Using Particles*, (Adam Hilger 1988).
- [41] R. Sperb, *Mol. Simul.*, **20**, 179 (1998).
- [42] M. Challacombe, C. White and M. Head-Gordon, *J. Chem. Phys.*, **107**, 10131 (1997).
- [43] J. Hautman and M. L. Klein, *Mol. Phys.*, **75**, 379 (1992).
- [44] D. M. Heyes, M. Barber and J. H. R. Clarke, *J. Chem. Soc., Faraday Trans. II*, **73**, 1485 (1977).
- [45] B. R. A. Nijboer, *Physica A*, **125**, 275 (1984).
- [46] A. Arnold and C. Holm, *Comput. Phys. Commun.*, **148**, 327 (2002).
- [47] E. Spohr, *J. Chem. Phys.*, **107**, 6342 (1997).
- [48] Y. J. Rhee, J. W. Halley, Joseph Hautman and A. Rahman, *Phys. Rev. B*, **40**, 36 (1989).
- [49] I. C. Yeh and M. L. Berkowitz, *J. Chem. Phys.*, **111**, 3155 (1999).
- [50] A. Arnold, J. de Joannis and C. Holm, *J. Chem. Phys.*, **117**, 2496 (2002).
- [51] J. de Joannis, A. Arnold and C. Holm, *J. Chem. Phys.*, **117**, 2503 (2002).
- [52] A. Bródka, *Chem. Phys. Lett.*, **410**, 446 (2005).
- [53] A. Arnold and C. Holm, *J. Chem. Phys.*, **123**, 144103 (2005).
- [54] L. Genovese, T. Deutsch, and S. Goedecker, *J. Chem. Phys.*, **127**, 054704 (2007).
- [55] M. Frigo and S. G. Johnson, *Proc. IEEE*, **93**, 216 (2005).
- [56] J. E. Flaherty, <http://www.cs.rpi.edu/%7Eflaherje/>
- [57] S. Adjerid, M. Aiffa, and J. E. Flaherty, *SIAM J. Appl. Math.*, **55**, 520 (1995).
- [58] B. Szabó and I. Babuška, *Finite Element Analysis*, (John Wiley & Sons, Inc. 1991).
- [59] T. Zykova-Timan, D. Ceresoli, U. Tartaglino, and E. Tosatti, *J. Chem. Phys.*, **123**, 164701 (2005).
- [60] J. Kolafa and J. W. Perram, *Mol. Simul.*, **9**, 351 (1992).
- [61] Walter Gander and Gene Howard Golub, in *Scientific Computing: Proceedings of the Workshop*, edited by Gene Howard Golub, Springer, pp. 73-76, (1988).

- [62] M. Abe and Y. Sugimoto and O. Custance and S. Morita, *Appl. Phys. Lett.* **87**, 173503 (2005).
- [63] M. Abe and Y. Sugimoto and O. Custance and S. Morita, *Nanotechnology* **16**, 3029 (2005).
- [64] Y. Sugimoto and P. Pou and O. Custance and P. Jelinek and S. Morita and R. Pérez and M. Abe, *Phys. Rev. B*, **73**, 205329 (2006).
- [65] Y. Sugimoto and P. Pou and M. Abe and P. Jelinek and R. Perez and S. Morita and O. Custance, *Nature* **446**, 64 (2007).
- [66] R. Pérez and M.C. Payne and I. Štich and K. Terakura, *Phys. Rev. Lett.* **78**, 678 (1997).
- [67] N. Oyabu and P. Pou and Y. Sugimoto and P. Jelinek and M. Abe and S. Morita and R. Pérez and O. Custance, *Phys. Rev. Lett.* **96**, 106101 (2006).
- [68] R. Pérez and I. Štich and M.C. Payne and K. Terakura, *Phys. Rev. B* **58**, 10835 (1998).
- [69] Y. Sugimoto and P. Jelinek and P. Pou and M. Abe and S. Morita and R. Perez and O. Custance, *Phys. Rev. Lett.* **98**, 106104 (2007).
- [70] N. Oyabu and O. Custance and I. Yi and Y. Sugawara and S. Morita, *Phys. Rev. Lett.* **90**, 176102 (2003).
- [71] F. Valiquette and N. Mousseau, *Phys. Rev. B* **68**, 125209 (2003).
- [72] A. Abdurixit, *Molecular dynamics simulations of noncontact atomic force microscopy and of relevant silicon systems*, 2000, PhD Thesis, University of Basel, Faculty of Science.
- [73] A. Abdurixit, A. Baratoff and E. Meyer, *Appl. Surf. Sci.* **157**, 355 (2000).
- [74] J. P. Perdew and A. Zunger, *Phys. Rev. B* **23**, 5048 (1981).
- [75] John P. Perdew, Kieron Burke, and Matthias Ernzerhof, *Phys. Rev. Lett.* **77**, 3865 (1996).
- [76] S. Kirkpatrick, C. D. Gelatt, Jr., and M. P. Vecchi, *Science* **220**, 671 (1983).
- [77] Thomas J. Lenosky, Joel D. Kress, Inhee Kwon, and Arthur F. Voter, *Phys. Rev. B* **55**, 1528 (1997).
- [78] J. C. Slater and G. F. Koster, *Phys. Rev.* **94**, 1498 (1954).
- [79] S. Goedecker and W. Hellmann, and T. Lenosky, *Phys. Rev. Lett.* **95**, 055501 (2005).

-
- [80] W. Hellmann, R. G. Hennig, S. Goedecker, C. J. Umrigar, B. Delley, and T. Lenosky, *Phys. Rev. B* **75**, 085411 (2007).
- [81] W. Hellmann, *Exploring the Born-Oppenheimer surface of small and medium-sized Si clusters using the dual minima hopping method*, 2007, PhD Thesis, University of Basel, Faculty of Science.
- [82] C. Z. Wang and C. T. Chan, and K. M. Ho, *Phys. Rev. Lett.* **66**, 189 (1991).
- [83] C. Z. Wang and K. M. Ho, *Adv. Chem. Phys.* **1996**, 651 (1996).
- [84] D. J. Wales and J. P. K. Doye, *J. Phys. Chem. A* **101**, 5111 (1997).
- [85] J. P. K. Doye and D. J. Wales, *Phys. Rev. Lett.* **80**, 1357 (1998).
- [86] J. Mestres, G. E. Scuseria, *J. Comput. Chem.* **16**, 729 (1995).
- [87] S. K. Gregurick, M. H. Alexander, and B. Hartke, *J. Chem. Phys.* **104**, 2684 (1996).
- [88] J. A. Niesse and H. R. Mayne, *J. Chem. Phys.* **105**, 4700 (1996).
- [89] D. M. Deaven and K. M. Ho, *Phys. Rev. Lett.* **75**, 288 (1995).
- [90] D. M. Deaven, N. Tit, J. R. Morris, and K. M. Ho, *Chem. Phys. Lett.* **256**, 195 (1996).
- [91] Stefan Goedecker, *J. Chem. Phys.* **120**, 9911 (2004).
- [92] F. Jensen, *Computational Chemistry* (Wiley, New York, 1999).
- [93] A. I. Livshits, A. L. Shluger, A. L. Rohl, and A. S. Foster, *Phys. Rev. B* **59**, 2436 (1999).
- [94] V. Caciuc, H. Hölscher, S. Blügel, and H. Fuchs, *Phys. Rev. Lett.* **96**, 016101 (2006).
- [95] P. V. Sushko, A. S. Foster, L. N. Kantorovich, and A. L. Shluger, *Appl. Surf. Sci.* **144-145**, 608 (1999).
- [96] R. Hoffmann, L. N. Kantorovich, A. Baratoff, H. J. Hug, and H.-J. Güntherodt, *Phys. Rev. Lett.* **92**, 146103 (2004).
- [97] A. S. Foster, C. Barth, A. L. Shluger, and M. Reichling, *Phys. Rev. Lett.* **86**, 2373 (2001).
- [98] T. Eguchi, Y. Fujikawa, K. Akiyama, T. An, M. Ono, T. Hashimoto, Y. Morikawa, K. Terakura, T. Sakurai, M. G. Lagally, and Y. Hasegawa, *Phys. Rev. Lett.* **93**, 266102 (2004).
- [99] T. Eguchi and Y. Hasegawa, *Phys. Rev. Lett.* **89**, 266105 (2002).

- [100] F. J. Giessibl, S. Hembacher, H. Bielefeldt, and J. Mannhart, *Science* **289**, 422 (2000).
- [101] R. García, R. Pérez, *Surf. Sci. Rep.* **47**, 197 (2002).
- [102] F. J. Giessibl, *Rev. Mod. Phys.* **75**, 949 (2003).
- [103] F. J. Giessibl, *Science* **267**, 68 (1995).
- [104] C. Loppacher, R. Bennewitz, O. Pfeiffer, M. Guggisberg, M. Bammerlin, S. Schär, V. Barwich, A. Baratoff, and E. Meyer, *Phys. Rev. B* **62**, 13674 (2000).
- [105] Peter M. Hoffmann, Steve Jeffery, John B. Pethica, H. Özgr Özer, and Ahmet Oral, *Phys. Rev. Lett.* **87**, 265502 (2001).
- [106] R. Hoffmann, M. A. Lantz, H. J. Hug, P. J. A. van Schendel, P. Kappenberger, S. Martin, A. Baratoff, and H.-J. Güntherodt, *Phys. Rev. B* **67**, 085402 (2003).
- [107] see, for instance, ch. 19 in Ref. [132].
- [108] M. Gauthier and M. Tsukada, *Phys. Rev. B* **60**, 11716 (1999).
- [109] L. N. Kantorovich, *J. Phys.: Condens. Matter* **13**, 945 (2001).
- [110] T. Trevethan and L. Kantorovich, *Nanotechnology* **15**, S44 (2004).
- [111] W. A. Phillips, *Rep. Prog. Phys.* **50**, 1657 (1987).
- [112] T. Trevethan and L. Kantorovich, *Phys. Rev. B* **70**, 115411 (2004).
- [113] T. Trevethan and L. Kantorovich, *Nanotechnology* **15**, S34 (2004).
- [114] A. Schirmeisen and H. Hölscher, *Phys. Rev. B* **72**, 045431 (2005).
- [115] B. Gotsmann, C. Seidel, B. Anczykowski, and H. Fuchs, *Phys. Rev. B* **60**, 11051 (1999).
- [116] B. Gotsmann and H. Fuchs, *Phys. Rev. Lett.* **86**, 2597 (2001).
- [117] W. Denk and D. W. Pohl, *Appl. Phys. Lett.* **59**, 2171 (1991).
- [118] J. Tamayo and R. García, *Appl. Phys. Lett.* **71**, 2394 (1997).
- [119] J. Tamayo and R. García, *Appl. Phys. Lett.* **73**, 2926 (1998).
- [120] L. N. Kantorovich, *Phys. Rev. B* **64**, 245409 (2001).
- [121] A. I. Volokitin and B. N. J. Persson, *Phys. Rev. Lett.* **91**, 106101 (2003).
- [122] J. B. Pethica and A. P. Sutton, *J. of Vac. Sci. and Technol. A* **6**, 2490 (1988).

-
- [123] V. Caciuc, H. Hölscher, S. Blügel and H. Fuchs, *Nanotechnology* **16**, S59 (2005).
- [124] J. P. Cleveland, B. Anczykowski, A. E. Schmid and V. B. Elings, *Appl. Phys. Lett.* **72**, 2613 (1998).
- [125] Andreas Heyden, Alexis T. Bell and Frerich J. Keil, *J. Chem. Phys.*, **123**, 224101 (2005).
- [126] R. Hoffmann, A. Baratoff, H. J. Hug, H. R. Hidber, H. v. Löhneysen and H-J Güntherodt, *Nanotechnology* **18**, 395503 (2007).
- [127] see, for instance, ch. 20 in Ref. [132]
- [128] L. N. Kantorovich and C. Hobbs, *Phys. Rev. B* **73**, 245420 (2006).
- [129] L. N. Kantorovich and T. Trevethan, *Phys. Rev. Lett.* **93**, 236102 (2004).
- [130] M. A. Lantz, H. J. Hug, R. Hoffmann, P. J. A. van Schendel, P. Kappenberger, S. Martin, A. Baratoff and H.-J. Güntherodt, *Science* **291**, 2580 (2001).
- [131] Y. J. Li, H. Nomura, N. Ozaki, Y. Naitoh, M. Kageshima, Y. Sugawara, C. Hobbs and L. Kantorovich, *Phys. Rev. Lett.* **96**, 106104 (2006).
- [132] S. Morita and R. Wiesendanger and E. Meyer, *Noncontact Atomic Force Microscopy*, Springer-Verlag, NanoScience and Technology, Berlin (2002).
- [133] L. Nony, A. Baratoff, D. Schär, O. Pfeiffer, A. Wetzler and E. Meyer, *Phys. Rev. B* **74**, 235439 (2006).
- [134] A. Ramstad, G. Brocks and P. J. Kelly, *Phys. Rev. B* **51**, 14504 (1995).
- [135] N. Sasaki and M. Tsukada, *Jpn. J. Appl. Phys.*, **39**, L1334 (2000).
- [136] T. Trevethan, M. Watkins, L. N. Kantorovich, A. L. Shluger, J. Polesel-Maris and S. Gauthier, *Nanotechnology* **17**, 5866 (2006) and references therein.
- [137] T. Trevethan and L.N. Kantorovich, *Nanotechnology* **17**, S205 (2006).
- [138] G. H. Vineyard, *J. Phys. Chem. Solids*, **3**, 121 (1957).
- [139] D. J. Wales, *Energy Landscapes*, Cambridge University Press, (2004).
- [140] K. A. Dill and S. Bromberg, *Molecular Driving Forces*, Garland Science, Taylor and Francis, London (2003).
- [141] M. Watkins and T. Trevethan and A. L. Shluger and L. N. Kantorovich, *Phys. Rev. B* **76**, 245421 (2007).

List of Publications

1. *Particle-particle, particle-scaling function algorithm for electrostatic problems in free boundary conditions.*
Alexey Neelov, **S. Alireza Ghasemi**, and Stefan Goedecker, J. Chem. Phys. **127**, 024109 (2007).
2. *A Particle-Particle, Particle-Density (P3D) algorithm for the calculation of electrostatic interactions of particles with slab-like geometry.*
S. Alireza Ghasemi, Alexey Neelov, and Stefan Goedecker, J. Chem. Phys. **127**, 224102 (2007).
3. *Ubiquitous mechanisms of energy dissipation in noncontact atomic force microscopy.*
S. Alireza Ghasemi, Stefan Goedecker, Alexis Baratoff, Thomas Lenosky, Ernst Meyer, Hans J. Hug
Phys. Rev. Lett. **100**, 236106 (2008).
4. *Daubechies wavelets as a basis set for density functional pseudopotential calculations.*
Luigi Genovese, Alexey Neelov, Stefan Goedecker, Thierry Deutsch, **Seyed Alireza Ghasemi**, Alexander Willand, Damien Caliste, Oded Zilberberg, Mark Rayson, Anders Bergman, and Reinhold Schneider.
J. Chem. Phys. **129**, 014109 (2008).
5. *Structure and stability of semiconductor tip apexes for atomic force microscopy.*
Pablo Pou, **S. Alireza Ghasemi**, Pavel Jelinek, Thomas Lenosky,
Stefan Goedecker, Rubén Pérez
Nanotechnology **20**, 264015 (2009).

Acknowledgments

I am indebted to University of Basel which provided me a valuable atmosphere during my education in University of Basel. I am grateful to all people who supported me during my PhD career. I would like to express my deep and sincere gratitude to my supervisor, Prof. Stefan Goedecker who was continuously encouraging and stimulating me. I wish to thank Dr. Alexis Baratoff for his extensive discussions around my work. Lastly, I am grateful to Prof. Ernst Meyer, the secretaries of physics department (Frau Audrey Fischer, Frau Astrid Kalt, Frau Barbara Kammermann), and Dr. Alexey Neelov.

Curriculum vitae

Name: Seyed Alireza Ghasemi
Date of Birth: 22nd March 1979
Place of Birth: Tehran, Iran

Education

Fall 1997 - Summer 2002:
B.Sc. in Physics at the Iran University of Science and Technology(IUST).

Fall 2002 - Summer 2004:
M.Sc. in Condensed Matter Physics at the Institute for Advanced Studies
in Basic Sciences(IASBS).

January 2005 - 2008 July:
Ph.D. in Computational Physics at the University of Basel.

List of Professors during my study at the University of Basel

Prof. Stefan Goedecker, Prof. Ernst Meyer, Prof. Alexis Baratoff, Prof. Hans Josef Hug

List of Professors and Lecturers during my studies at the IUST and IASBS

Mr. Haik Gholtoghchian, Prof. Mohammad Reza Rahimi Tabar, Prof. Mohammad
Khorrami, Prof. Abdollah Langari